Spatial diagnostics of plasma produced by a VHF multi-tile electrode

A thesis submitted for the degree of

Master of Science

Kevin Ryan

School of Physical Sciences

Dublin City University

Research Supervisor: Dr A.R Ellingboe

External Examiner: Dr S. Shannon

Internal Examiner: Dr S. Daniels

April 2012

I hereby certify that this material, which I now submit for assessment on the programme of study leading to the award of Masters of Science, is entirely my own work, that I have exercised reasonable care to ensure that the work is original, and does not to the best of my knowledge breach any law of copyright, and has not been taken from the work of others save and to the extent that such work has been cited and acknowledged within the text of my work.

Signed: ______________ (Candidate) ID No.:______________ Date: ___________

Kevin Ryan

Plasma Research Laboratory,

School of Physical Sciences,

Dublin City University,

Dublin, Ireland.

Abstract

A scalable multi-tile electrode plasma source operating at 150MHz and 162MHz is described. An investigation into the spatial structure of plasmas produced in such as source is reported. Four different plasma diagnostics are applied to examine this spatial structure; they are time-varying magnetic flux probe measurements of the magnetic flux, planar Langmuir probe measurements of the ion saturation current density, capacitive probe measurements of the plasma oscillation potential and measurement of *rf* current and voltage on tiles. Spatial profiles of the plasma potential oscillation and the ion saturation highlight the spatial structure imposed on plasmas produced in the PASTIS source. Analysis of the *rf* tile current and voltage in the segmented electrode array yields information on the nature of the impedance of both the source and plasma. *rf* currents in the tiles cause a magnetic dipole to be induced in the regions between tiles. Thus, although the PASTIS source is a capacitive discharge, we must consider a model that includes both capacitively and inductively coupled plasma. This induced dipole moment is measured with a specifically designed VHF time-varying magnetic flux probe. Analysis of the diagnostics presented show that there is a well defined spatial structure imposed on the plasma by the segmented electrode tile array.

Acknowlegements

I would like to show my appreciation and gratitude to Dr Bert Ellingboe for his continued guidance support and encouragement through out the duration of my research. His depth of knowledge, experience and his uncanny ability to help solve many of the unique problems encountered during this project have proved to be invaluable. His leadership as head of the Plasma Research Laboratory in DCU has inspired me to pursue my research interests.

To all current and past members of the Plasma Research Laboratory; Cezar, Dave, Eamonn Tom, Daniel and Tom, it has been an absolute pleasure to work with you all. To Tomasz, Neal and Fiachra and all who I worked with at *Phive*, I wish you all the best

My sincerest thanks go the academic and technical staff and students here in DCU for the unending assistance they provide. Specifically I would like to mention Prof. Greg Hughes, Mr. Des Lavelle, Mr Pat Wogan, Mr Henry Barry and Ms Lisa Peyton.

I would like to take this time to thank my family for supporting my decision to pursue my research; you will never know how much your never ending encouragement and advice means to me.

Finally I would like to thank my closest friends, Rónán, Dee, Andrew, Louise, Ian, Alan and Jen. I am eternally grateful for the moral support and many welcome distractions you have all provided to me during my research. I dedicate this thesis to you all.

Contents

List of Figures

Chapter 1

Introduction

1.1 Introduction to Plasmas

The change from solid to liquid to gas with increased temperature (energy) is a phenomenon with which everyone is familiar. Traditionally referred to as the three *"states of matter"*, the physical properties of a solid, liquid and gas are different. A further addition of energy to matter in the gaseous phase can cause collisions between the atoms/molecules that, cause it to become ionized.

$$A + B + Energy \Rightarrow A + B^{+} + e^{-} \tag{1.1}$$

Plasma is defined as an ionized gas that exhibits collective behavior. The behaviour of "plasma," particularly in response to electric and magnetic fields differs from that of a solid, liquid or gas and thus, "plasma" is considered by many to be be the fourth state of matter.

Plasma is in fact the most common form of matter in the visible universe. Most stars, including our own Sun are examples of plasma. The Aurora Borealis, arc welders, neon signs and even florescent lights are more common examples of plasmas with which we are all familiar.

Consider, a weakly ionized gas ($<\sim 0.1\%$) containing electrons, ions and neutrals, all in a steady state, confined in a grounded, conductive box at a pressure in the order of approximately 100mTorr. We further assume that the electron density (n_e) and ion density (n_i) is equal such that the total net charge of the gas is zero.

$$n_e \approx n_i = n_0 \tag{1.2}$$

This is called quasi-neutrality. Where n_0 is called the plasma density.

Suppose that all particles have a thermal distribution that obeys a Maxwell-Boltzmann distribution at time $t = 0$ such that

$$T_e \gg T_i \simeq T_n \tag{1.3}$$

i.e. the electrons have a much higher temperature than both the ions and neutral species in our plasma, and thus are not in thermal equilibrium with them. The thermal velocities of the electrons and ions is then

$$v_{th,e} \gg v_{th,i} \simeq 0. \tag{1.4}$$

Advancing the system by a time Δt, some of the electrons within a distance Δx of the boundary (where $\Delta x = v_{th,e}\Delta t$) strike the boundary and the charge is absorbed. There is then a resulting deficit of electrons within this region Δx near the wall.

Integrating the charge over position from the grounded boundary into the plasma, the excess of positive ions in this region gives rise to a positive potential for the plasma. This positive potential acts to accelerate ions in this edge region and prevents low energy electrons

$$\frac{1}{2}m_e v_e < (V' - V_{GND}) \tag{1.5}$$

from reaching the wall.

Carrying forward in time, this edge region with an excess in ion density grows with V' until the flux of electrons is reduced to match the flux of the ions. Thus resulting in a steady-state condition where the plasma potential, $V_p \simeq 3.5 \times k_B T_e$. This boundary region over which the plasma is no longer quasi-neutral, acts to maintain a balance of charge within the plasma bulk, and is called the sheath.

1.1.1 Particle transport in the plasma sheath and the application to Langmuir probes

Suppose that there is an equal number of ions and electrons in the bulk plasma and that both ions and electrons have an even spatial distribution. If we introduce an unbiased floating electrode into the plasma, as shown in figure 1.1, we bring about a disturbance to the local electric field around the electrode. Using Poissons equation in one dimension,

$$\nabla \cdot E = \frac{d^2V}{dx^2} = \frac{\rho_f}{\epsilon} \tag{1.6}$$

to define the change of potential V as a function of distance from the electrode. Where ρ_f is the charge density on the surface of the probe. Equation 1.4 allows us to assume the ions are fixed, and that only the electrons are affected by the potential, thus the Poisson equation becomes,

$$\frac{d^2V}{dV^2} = -\frac{e}{\epsilon_0}\left(n_i - n_e(x)\right) \tag{1.7}$$

For electron densities described by a Maxwellian distribution,

$$n_e\left(x\right) = n_0 e^{\frac{e\left(V(x)-V_p\right)}{kT_e}} \tag{1.8}$$

Using the Taylor expansion to the second order,

$$n_e(x) = n_0 \left[1 + \frac{eV(x)}{kT_e}\right] \tag{1.9}$$

Subbing in and simplifying for n_e, the Poisson equation becomes,

$$\frac{d^2V}{dx^2} = -\frac{en_0}{\epsilon_0}\left(1 - e^{\frac{eV(x)}{kT_e}}\right) \tag{1.10}$$

For $V(x) \ll kT_e$, equation 1.10 simplifies to

$$\frac{d^2V}{dx^2} = \frac{en_0}{\epsilon_0}\frac{eV(x)}{kT_e} \tag{1.11}$$

which when integrated becomes,

$$V = V_0 e^{\left(-\frac{|x|}{\lambda_D}\right)} \tag{1.12}$$

where,

$$\lambda_D = \sqrt{\frac{\epsilon_0 kT_e}{e^2 n_0}} \tag{1.13}$$

is the Debye length, and in effect, defines the quasi-neutrality limit, i.e. a plasma of characteristic length L is considered to be quasi-neutral if the inequality $\lambda_D \ll L$ is true.

For a floating electrode when steady state has been reached the flux of electrons reaching the electrode are necessarily equal.

$$\Gamma_e = \Gamma_i \tag{1.14}$$

where

$$\Gamma_e = n_0 e^{\left(\frac{-eV - V_p}{kT_e}\right)} v_{e,th} \quad \text{and} \quad \Gamma_i = n_0 v_{ion}. \tag{1.15}$$

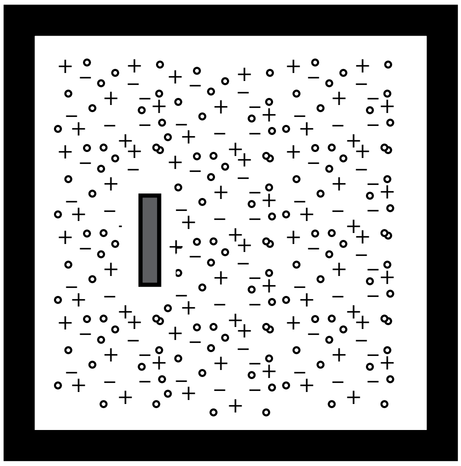

Figure 1.1: Unbiased electrode immersed in a plasma [1]

As described above, within a very short period of time an ion rich sheath forms around the electrode, in order to maintain a balance of charge.

We define the potential difference between this electrode and ground as the plasma potential V_p.The measured current is the sum of electron and ion fluxes striking the surface of the electrode.

$$I = e\left(\Gamma_i - \Gamma_e\right) \tag{1.16}$$

Instead of grounding this electrode, next we consider what would happen if we were to connect it to a variable voltage supply, as shown in figure 1.2 and plot a graph of current versus voltage applied to the electrode (figure 1.3). Applying a potential bias, such that $V_{bias} - V_p > 0$, the resulting electric field points away from the biased electrode and into the plasma thus retarding the flux of “cold” ions to the electrode.

Lets now decrease the bias voltage such that $V_{bias} - V_p < 0$ so that the resulting electric field points towards the probe. Now positive ions are accelerated towards the electrode and the flux of electrons is completely suppressed. The measured

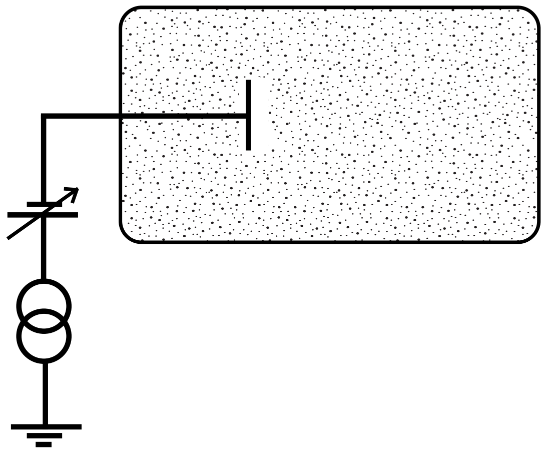

Figure 1.2: Biased electrode inserted into a plasma [1]

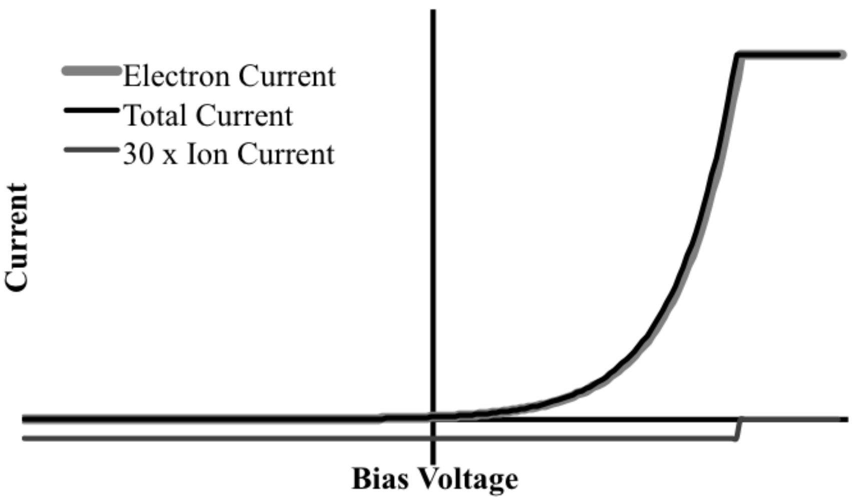

Figure 1.3: Typical graph of current versus electrode voltage profile in a plasma [1]

current is due only to positive ions and is called the ions saturation current. This is the main principle of operation of a Langmuir probe and is described in greater detail in section 3.5. Figure 1.3 shows a typical graph of current vs electrode voltage in a plasma.

Effect of an oscillating electrode voltage on the plasma

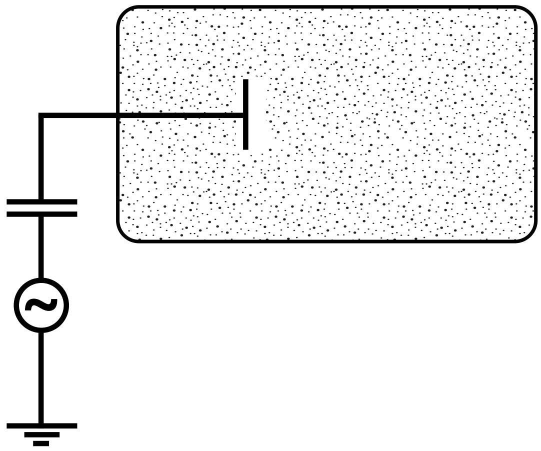

Figure 1.4: Electrode with a oscillating bias voltage inserted into the plasma. A blocking capacitor is connected in series to the voltage source to ensure that only the sinusoidal current flows to the electrode surface. [2, 1]

Suppose a small sinusoidal voltage, oscillating around the floating potential is applied to the electrode in figure 1.4. We assume that electrons respond instantaneously to the phase of the oscillating probe voltage. Ions are much heavier and have a sluggish response and so their velocity can be considered to be almost constant over an *rf* cycle. As $V_{bias} < V_p$, the ion current to the electrode is the same as the ion saturation current defined above. Figure 1.5 shows, the density of ions and electrons in the sheath as a function of position, (x) and *rf* phase (ϕ) and highlights the evolution of the electron density in the sheath over the *rf* cycle.

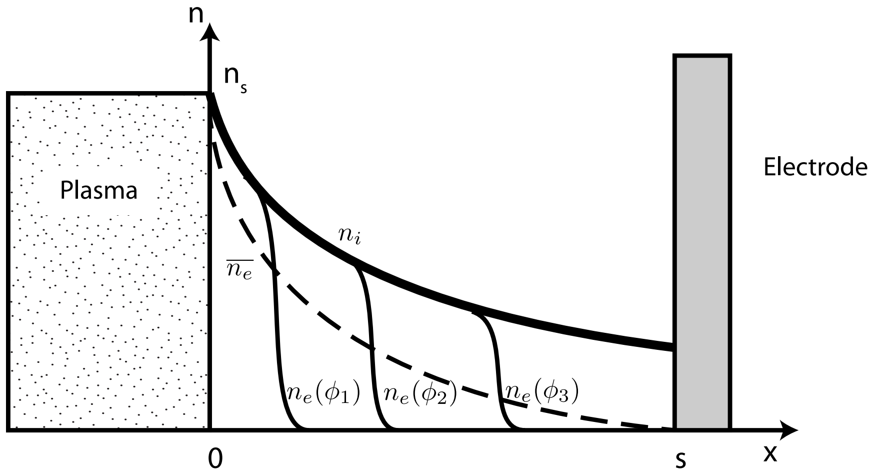

Figure 1.5: Density of charged species versus distance from the sheath edge. The instantaneous electron density is a function of both position and *rf* phase [2]. $\phi_1 = \frac{\pi}{4}, \phi_2 = \frac{\pi}{2}$ and $\phi_3 = \frac{3\pi}{4}$.

Considering electron current during the positive half of the sinusoidal cycle, we note that the electron flux is accentuated. Electron flux is suppressed during the negative half of the cycle. However, because electron flux responds exponentially as a function of bias voltage, integrating over a full cycle of oscillation (period) reveals that more electrons are incident on the electrode surface than without an oscillating bias.

This has the resulting effect of placing a negative self bias on the probe which will cause a reduction in electron flux, such that the integrated electron flux over one period equals the time averaged ion flux, as the probe is positive for a smaller fraction of each period.

$$\int_0^{2\pi} I_e(\omega)\, d\omega = \overline{I_i} \tag{1.17}$$

This self bias has the effect of balancing the current into the plasma, thus preventing further charge imbalance. Increasing the amplitude of the oscillating bias will result in a greater self bias. The electron saturation current is sufficiently large that the peak *rf* voltage will never exceed the plasma potential. Thus, the assumption of a constant ion flux is valid as the sheath voltage is constantly accelerating ions to the boundary.

1.1.2 Natural frequency of oscillation in the plasma

In the above section we assumed that the response of the electrons to the oscillating bias voltage is immediate and independent of the oscillation frequency. However as the frequency of oscillation increases we will approach a state where the inertia of the electrons causes a lag in their response to the changing bias. We can deduce the frequency at which this occurs by determining the natural frequency response of the electrons

Assuming that within the bulk plasma, ions are fixed and evenly distributed in space, then from quasi-neutrality, we see that the net electric field within the plasma is zero. However, lets suppose that and electric field is imposed on the plasma. As consequence, electrons are displaced by a small distance Δz to the left. This would result in a positive surface charge imbalance on the right equal to $n_e \Delta z$ and as a result, a positive electric field on the side of the plasma, as there is a surplus of ions. Conversely on the opposite side, there would be a deficit of ions and therefore a negative electric field [1].

Due to this displacement, a restoration electric field appears. The electrons reverse their trajectory, but they pass the starting point because of the inertia. Thus, the electrons oscillate with a frequency depending on the restoration electric field.

We can use the Poisson equation (1.6) to define the electric fields caused by the displacement Δz.

$$\frac{dE}{dz} = \frac{n_0 e}{\epsilon_0} \tag{1.18}$$

which when integrated becomes,

$$\vec{E} = \frac{n_0 e}{\epsilon_0} z \tag{1.19}$$

The equation of motion of the electrons is then described by

$$\begin{aligned} F = e\vec{E} &= ma && (1.20) \\ m_e \frac{d^2 z}{dt^2} + \frac{n_0 e^2}{\epsilon_0} z &= 0 && (1.21) \end{aligned}$$

Note that this equation has the form of the equation describing an undamped simple harmonic oscillator with an electron oscillation frequency given as

$$\omega_e = \sqrt{\frac{n_0 e^2}{\epsilon_0 m_e}} \tag{1.22}$$

In reality, both ions and electrons oscillate around their common center of mass. However, because $m_{ion} \gg m_{electron}$, the assumption that the ions are stationary and that the electrons oscillate with respect to the ions is highly accurate. This assumption is justified by equation 1.23:

$$\mu = \frac{m_1 m_2}{m_1 + m_2} = \frac{1 \times 1836}{1 + 1836} = \frac{1836}{1837} = 0.9995 m_e \tag{1.23}$$

Equation 1.22 shows that the natural frequency of a plasma has a square root dependance on the plasma density. So for a plasmas density of 10^9 cm^{-3}, the natural frequency is about 280 MHz. Similarly a plasma with a density of 10^{10} cm^{-3} will have a frequency of approximately 900 MHz, while the plasma frequency is almost 3 GHz for discharges with a density greater than 10^{11} cm^{-3}.

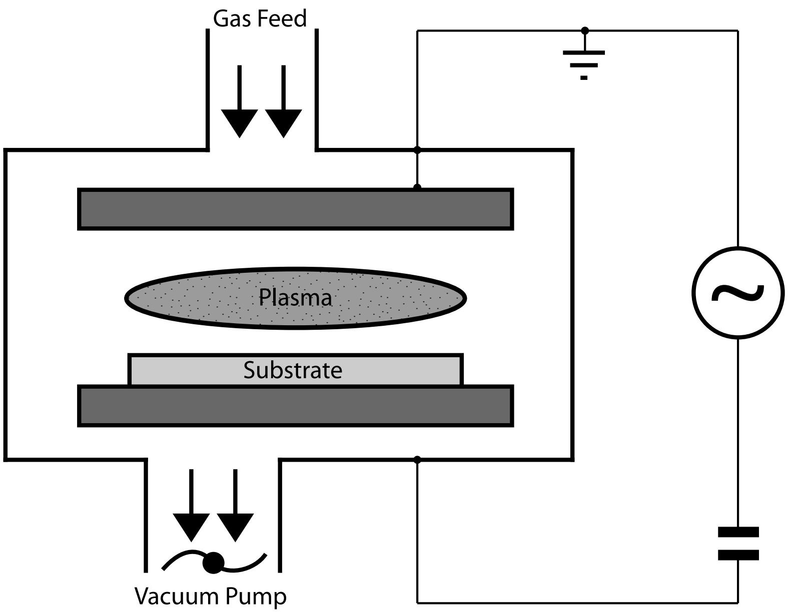

Figure 1.6: Schematic of a capacitively coupled plasma source.

1.2 Plasma Sources

1.2.1 CCP Sources

One of the most widely used plasma sources in industry is the capacitively coupled discharge. Figure 1.6 shows a typical CCP source. In essence, a CCP source consists of two parallel electrodes, separated by a dielectric medium, the plasma. The two electrodes and the plasma volume are contained within an insulating vacuum chamber. The name is a derivation of the similarity of this configuration to that of a capacitor. With applications in the semi-conductor, photovoltaic and surface treatment sectors, there is a lot of interest in the development of CCP sources.

Power is typically delivered to the system by means of a differential sinusoidal voltage (usually 13.56 MHz) which is applied to the one electrode while the other is grounded. It is however, not uncommon to find CCP discharges in which both electrodes are powered. When *rf* power is applied, a strong electric field forms between the powered and ground electrodes and any free charges within the gas volume are accelerated, causing the gas to break down and a plasma to form between the electrodes. A thin sheath separates the electrodes from plasma bulk.

If the applied sinusoidal voltage is driven at a low frequency (1kHz $\leq \omega_{rf} \leq\sim 5MHz$), the system can be likened to a DC discharge with two resistive sheaths. Ions are assumed to be unaffected by the changing electric field and so are considered to be be fixed with a constant outward flux to the walls and the powered electrodes.

On the other hand, the electrons respond quickly to the changing electric field. As the time dependent voltage changes during the *rf* cycle, the voltage of the sheath drops below zero. Figure 1.7 shows that there is a loss of electrons on one side of the plasma during the negative part of the *rf* cycle due to the changing potential during the *rf* cycle. As the *rf* phase becomes positive again, this effect is observed on the opposing electrode. Therefore while there is a constant flux of ions accelerated out of the plasma, the electron loss has a spatial dependence depending on the phase of the *rf* cycle.

Power coupling between the electrodes and the plasma is generally assumed to be purely capacitive at lower frequencies - i.e. the electric field is normal to the plane of the electrodes.

1.2.2 ICP

The inductively coupled discharge is another commonly used plasma source. There are generally two configurations of ICP discharges; planar and cylindrically coiled. The coil of a planar ICP is wound flat - similar to that of a kettle heating element, while the windings of a cylindrical discharge resemble that of a spring. Both coil geometries are powered by applying an *rf* current through the coils to induce image currents within the plasma volume thus ionizing the gas

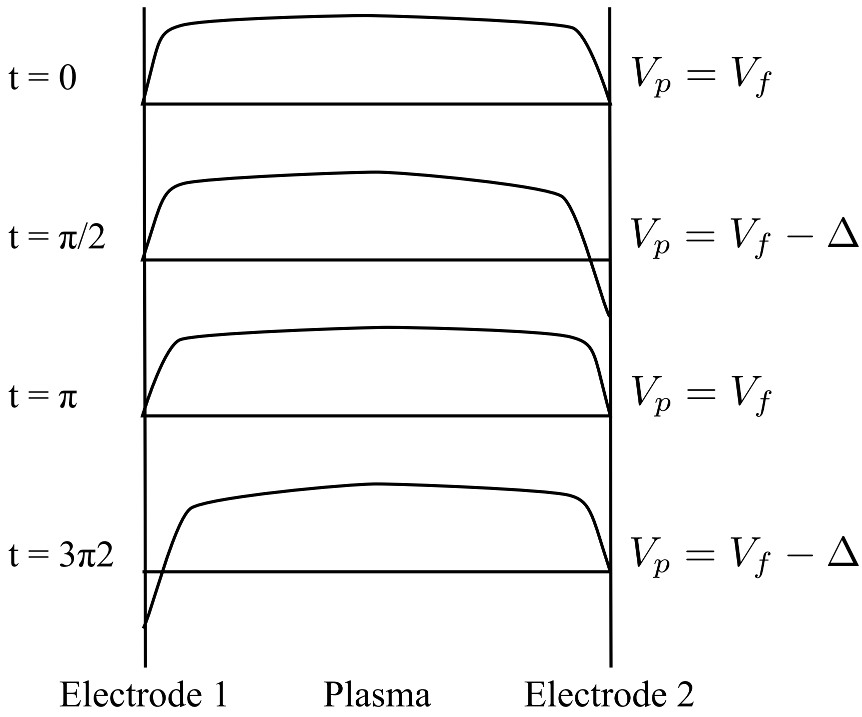

Figure 1.7: Spatial variation of the potential in a parallel plate CCP, at four different phases in the rf cycle

and creating a plasma.

In contrast with CCP's, the powered coils are not in direct contact with plasma. As a result they are often used for industrial applications where reduced contamination of the plasma species is a requirement. The rf magnetic field induced by the coils penetrates into the plasma. Because the plasma is also a conductor, currents are induced within the plasma. These currents flow in a direction opposite to that of the coils so as to shield the magnetic field from the bulk plasma. These induced "image" currents scale with the skin depth

$$\delta = \frac{c}{\omega_{pe}} = \sqrt{\frac{2\rho}{\omega\mu}} \tag{1.24}$$

where ω_{pe} is the plasma frequency which we defined earlier (equation 1.22) to be proportional to the square root of plasma density, ρ and μ are the resistivity and

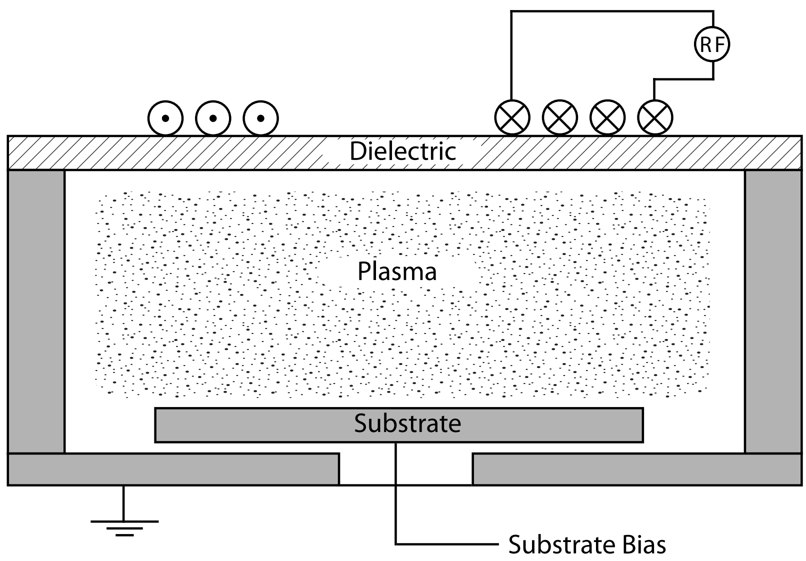

Figure 1.8: Schematic of a inductively coupled plasma source

relative permeability of the plasma.

1.2.3 VHF CCP with inductive power coupling on edge

The standard industrial *rf* power driving industrial plasma's is 13.56 MHz , however it has been shown that scaling to VHF/UHF frequencies has many advantages [3], such as reduced ion bombardment energy at a higher ion flux [4, 5]. This is desirable in PECVD of micro-crystalline Silicon applications where the high density enables a faster rate of deposition while the lower energy ions do not cause amorpization of the micro-crystalline Silicon layer, thus maintaining a high film quality.

Recall from equation 1.24, that the skin depth in a conductor is shorter at higher frequencies,

$$\delta = \frac{c}{\omega_{pe}} = \sqrt{\frac{2\rho}{\omega\mu}}.$$

In typical conductors the skin depth, δ, at VHF frequencies, is in the order of

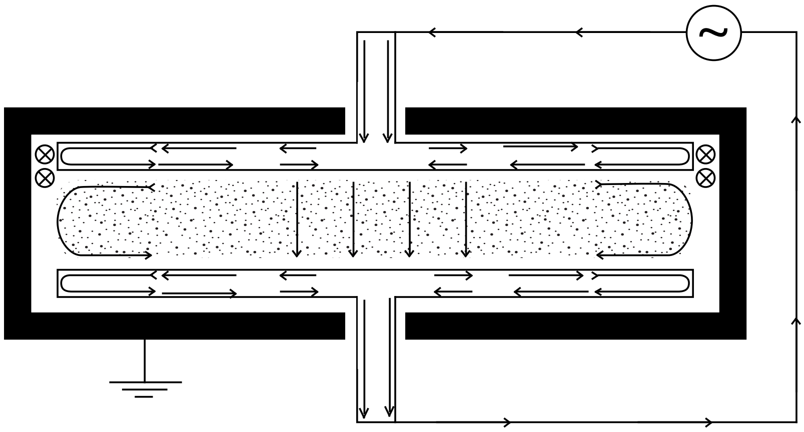

Figure 1.9: Schematic showing surface currents, capacitvely coupled currents and induced image currents in a VHF CCP discharge

microns, so current flows along the surface.

Figure 1.9 shows a cross-section of a simple capacitively coupled system showing the instantaneous current vectors. Currents flowing around the edge of the electrode, cause image currents to be induced in the plasma. Consequently, in VHF CCP discharges, power is coupled into the plasma, both capacitively and inductively [6, 7].

Additionally, image currents in the grounded chamber wall are also induced near the edge of the electrode. This causes a magnetic dipole moment to form between the edge of the electrode and the chamber wall which acts to draw more current to the electrode edge.

The effect of this edge inductive coupling is the presence of spatial non-uniformities in the electric field density between the edge of the plasma and the center of the electrode. The electric field is normal to the electrode surface at the centre of the discharge and at the edge, there are two components; a capacitive element, perpendicular to the boundary, which is proportional to the voltage as a function of time and an inductive component parallel to the boundary that is proportional to the time varying current.

Furthermore, as substrate sizes increase for faster industrial throughput and higher efficiency, the wavelength of the VHF driving voltage is now on the same scale as the source geometry. This results in the formation of standing waves on the electrode surfaces causing further plasma non-uniformities across the plasma volume.

1.3 Thesis Structure

After an overview of the experimental setup in Chapter 2, a description of the theory behind diagnostics used is given in Chapter 3. Numerical and Analytical results of the data collected is provided in chapters 4 and 5. Finally conclusions and possible future work is discussed in the final chapter.

Chapter 2

Experiment

2.1 Multi-tile segmented electrode VHF/UHF CCP sources

In CCP discharge operating in VHF, the inductive electric field causes currents to flow around the edge of the discharge. Consequently, controlling the plasma parameters at high frequency becomes difficult. By dividing the powered electrode into an array of individual tiles, each powered 180° out of phase with adjacent tiles, a large area, high frequency scalable plasma source can be achieved [8].

The wavelength effects mentioned in section 1.2.3 are dependent on the size of the electrode. Thus by keeping the individual tiles much smaller than the wavelength of the driving *rf* power, wavelength effects can be minimized.

Figure 2.1 shows a pair of differentially powered tiles above a plasma. By powering neighbouring tiles 180° out of phase, in a *push-pull* configuration, the instantaneous net current from the electrode array to ground at any given *rf* -phase is zero. In addition to this, the inductive coupling between tiles occurs in the plane of the tile array. This means that a more dense plasma can be produced. A more complete description of the how power is delivered to tiles is outlined in

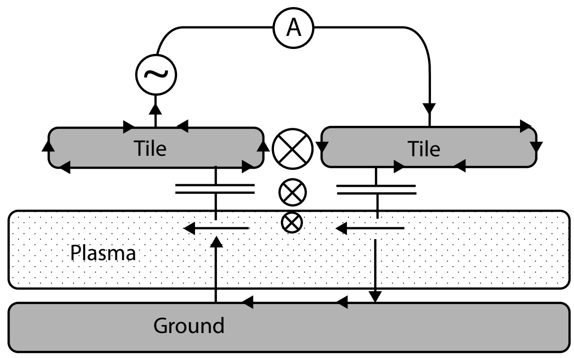

Figure 2.1: Showing the current and magnetic vectors in a multi-tile discharge

section 2.3

2.2 Description of PASTIS plasma source

The PASTIS plasma source used in this experiment is a multi-tile electrode source, a rectangular system, consisting of a 3×4 array of 10×10 cm square aluminum tiles. A 1cm wide alumina inter-tile ($\epsilon_r \simeq 10$) dielectric exists in between tiles, which means that the resulting electrode size is 45×34 cm. The plasma volume is 47cm by 35cm by 5.5cm high. Figure 2.2 shows a cross section schematic along the long 4 tile axis of the system. On the back side of the electrode tile array, is a low ϵ_r *PEEK* insulator separating the electrodes from a ground plate.

Individual tiles are identified using a letter/number scheme where the letters A, B and C refer to the position of tiles on the short axis, and the numbers 1, 2, 3 and 4 refer to the position in the long axis of the tile array. For example, tile B4 is the 4th tile in the center row. Figure 2.3 shows the electrode array with the labeled tiles

A shower head structure in each of the tiles, enables a uniform gas delivery to the plasma volume. Above the ground plate, exists a pumping plenum, which

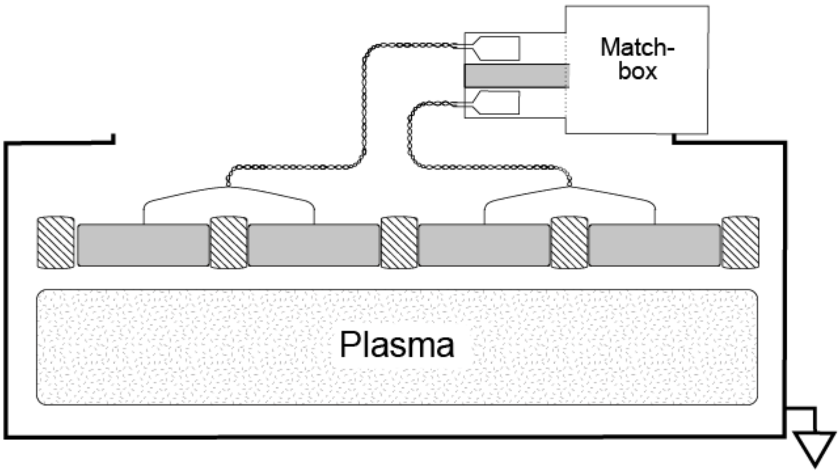

Figure 2.2: The PASTIS multi-tile electrode source

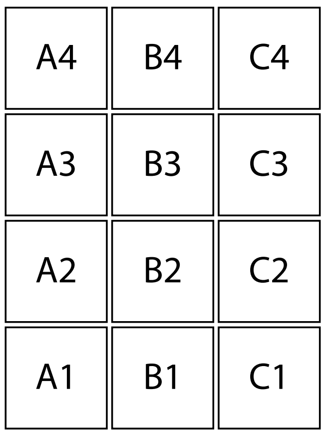

Figure 2.3: The naming convention used for the tiles on PASTIS

is pumped by a turbomolecular pump below the chamber. Gas flows from the plasma volume to the pumping plenum through 1mm slots in the alumina inter-tile dielectric and a 1mm gap between the wall and the electrode array.

rf power is applied to the system via an ENI Genesis 150 MHz generator which has a maximum output power of 2 kW.

2.3 Power Splitting and matching network

The *rf* power from the generator needs to be divided equally among the tiles in the antenna array. This is achieved using a Power Splitting Transmission Line Device or PSTLD[9, 10]. A PSTLD consists of two concentric metal cylinders, to form a coaxial transmission line. An annular conductive end plate connects the two cylinders, forming and electrical short. A number of coupling loops are inserted, through holes in the end plate, into the cavity between the two cylinders. Theses loops are orientated in such a way that the normal to the plane of the loop is parallel to the tangent of the wall of the transmission line. When *rf* power is applied to the inner conductor of the transmission line, an oscillating magnetic field is formed in the azimuthal direction. This oscillating azimuthal field passes through the coupling loops, inducing a time varying voltage as per the Maxwell Faraday equation.

$$\nabla \times E = -\frac{dB}{dt}. \tag{2.1}$$

Integrating over the defined path-length of the secondary loop gives the time varying differential potential at the two ends of the secondary loop at the feedthru in the end plate of the primary transmission line.

$$\frac{d\Phi}{dt} = \frac{\delta}{\delta t}\left(\vec{B} \cdot \vec{A}\right) \tag{2.2}$$

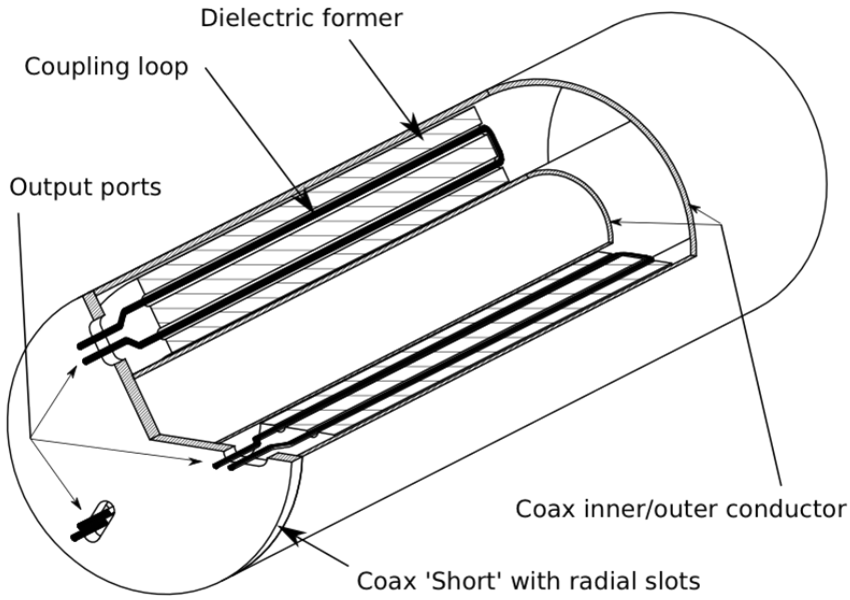

Figure 2.4: A cross section depiction of a 6-way PSTLD

The coupling loops are connected to pairs of tiles by twisted pair transmission line. This induced voltage in the coupling loops drives push-pull power to the tiles differentially through the twisted pair transmission line.

rf power is provided to the PASTIS system by an ENI Genesis 150MHz generator via a matching network. Power is delivered to each tile by the PSTLD. This configuration is actually analogous to an *rf* transformer where the magnetic field produced by a primary (the coaxial transmission line) induces a voltage in a secondary winding (the coupling loops). The power coupled, to each loop and therefore to the tile pairs, is determined by the number of loops and the area enclosed by each loop. Similarly, for a PSTLD with N equally sized coupling loops, the power coupled to each loop is split equally.

One of the resulting effects of differentially powered push-pull tile pairs is that each tile is 180° out of phase with its pair. The power is delivered to the tile pairs, subsequently, the power is shared between the tiles. As a result, there is *zero* net current in the system.

The PASTIS source electrode array consists of 12 tiles, or 6 tiles pairs. This means that there are six coupling loops inside the PASTIS PSTLD.

As the impedance of the system will change with the presence of plasma, a matching network is installed to tune the impedance of the system to 50 Ω

2.4 Experimental operating conditions

Data is typically collected in Argon plasmas at pressures in the range of 5 mTorr and 500 mTorr a powers between 100 W and 1.5 kW. Spatial profiles and power scans were carried out at a variety of fixed pressures in PASTIS

2.5 Data acquisition and automation

A PC running LabVIEW acts as a control interface for the experiment. A 64 channel data acquisition (DAq) board connects the experiment to the PC. The LabVIEW programme reads in the signals from the board at a resolution of up to 10000 Hz. However due to memory limitations of the PC, experiments were mostly carried out with a reduced acquisition resolution of 1000 Hz.

The power set point for the ENI Genesis generator is determined by the user. In addition to this, LabVIEW also monitors the the forward and reflected power via the 64 channel DAq board.

rf probe measurements are processed using a pair of Stanford Research $SR-844$ Lock-in Amplifiers. An brief overview of the techniques used for *rf* diagnostics will be provided in section 3.1. Each lock-in amplifier converts the raw probe signal into a pair of 0-10 V DC voltages which are connected to the 64 channel DAq board. Langmuir probe signals are DC only and thus are connected directly to the DAq board.

The position of the plasma probes is recorded using a length of non-elastic nylon thread, wrapped around a teflon wheel attached to a 10 turn potentiometer conncected to a 9 V battery. As the probe is manipulated, the teflon wheel rotates, changing the voltage across the 10-turn pot. This voltage is recored using the 64 channel DAq board

Chapter 3

Plasma Diagnostics

3.1 General overview of the techniques for *rf* diagnostics

When analysing *rf* signals, both the amplitude and the phase of the signal are of importance. As described in Section 2.5, a pair Stanford Research $SR-844$ lock-in amplifiers are used to analyse the probe signals.

The amplitude of the measured signals is calculated as

$$A = \sqrt{X^2 + Y^2} \tag{3.1}$$

where $X = A \cdot sin\theta$ and $Y = A \cdot cos\theta$, the X and Y output DC signals from the $SR-844$ lock-in amplifier [11].

The phase of both the current and voltage is calculated as,

$$\theta = tan^{-1}\left(\frac{X}{Y}\right) \tag{3.2}$$

The exact phase relationship between the instantaneous probe signal in comparison to the signal input into the lock-in is not known. Thus to enable relative phase measurements, phases of rf signals are measured with respect to a reference. The reference chosen is a $\dot{B}$ probe inserted into the co-axial section of the matchbox.

Note that none of these phase delays from the source of the signal to the lock-in has an absolute calibration. By comparison to a common standard, changes in phase difference between two signals is achieved. Absolute calibration of the phase difference between the antenna current and voltage on a given tile is achieved by collecting a measurement in vacuum.

3.2 Capacitive Probes

Due to the multi-tile configuration of the PASTIS source, a spatial structure is imposed on the plasma. A capacitive probe is used to obtain spatially resolved profiles of the phase and amplitude of the plasma potential oscillation.

A capacitive probe consists of a co-axial transmission line with a conductive electrode attached the end of the inner conductor placed inside a re-entrant quartz tube inside the plasma volume. When inserted into the plasma, the quartz tube is charged by the plasma to the floating potential [12]. The electrode is then capacitively coupled to this floating potential [13].

The capacitive probe used to measure the plasma potential oscillation in PASTIS consists of a RG-58 co-axial transmission line with a 10 mm long $\times$ 5 mm diameter, copper probe tip soldered on to the end of the center conductor.

Because the sheath capacitance between the probe tip and the plasma has a finite impedance, we can consider the probe to have an equivalent circuit to that of a capacitive-voltage divider as shown in figure 3.1. The walls of the quartz tube are 1mm thick, thus limiting the radial variance (Δr) of the 5mm probe tip to $\pm$1mm. For a Δr within the bounds of the quartz tube, there is a negligible change in the capacitance between the outer surface of the quartz tube and the

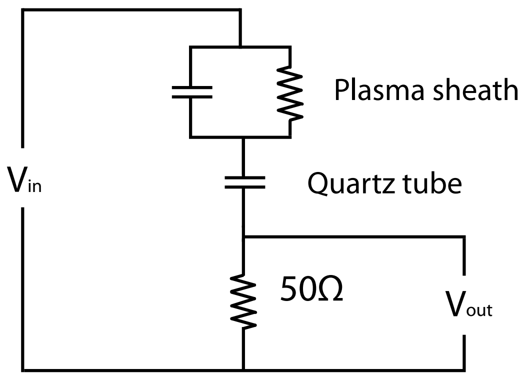

Figure 3.1: Equivalent circuit of a capacitive probe

surface of the probe tip. Similarly, a small variation in the thickness of the walls of the quartz tube will have little effect on the floating potential measurement.

A 50 Ω resistor connects the center conductor with the outer conductor in order to provide impedance matching and increase the transmission of VHF/UHF harmonics of the plasma potential oscillation. Figure 3.2 depicts the copper probe tip with the 50 Ω resistor connecting the center conductor to the outer. The length of the probe is 1080 mm .

Previous work [14] found that because such a large area of the outer conductor of the co-ax cable is exposed to the plasma volume and that the length of the ground shield between the probe tip and the connection to true experimental ground is a large fraction of a quarter wavelength, the outer conductor also couples capacitively to the VHF electric fields within the plasma. This results in a voltage oscillation in the ground shield which adds to the V_{out} at the output coupling resistor, thereby giving misleading and/or incorrect values of the potential at the probe tip. In order to overcome this, a tri-axial cable is used instead [15, 16]. The outer conductor shields both center conductors from rf coupling and the voltage measured between the two center conductors represents the plasma potential oscillation.

The probe is inserted into a re-entrant quartz tube and manipulated across

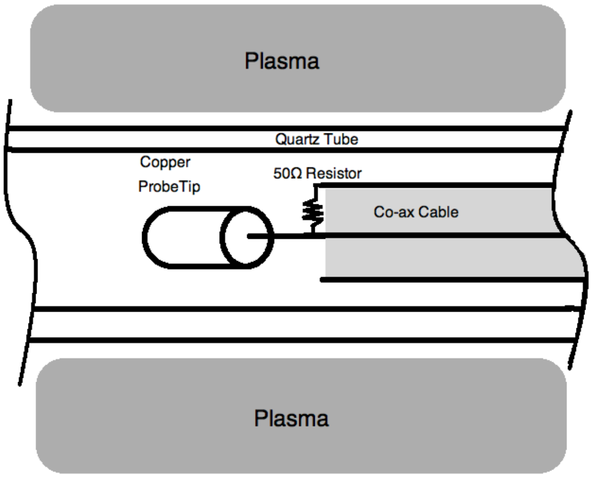

Figure 3.2: Capacitive probe showing copper probe tip and $50\,\Omega$ resistor

the long axis of the PASTIS chamber. As a result, the values measured provide only a qualitative representation of the plasma potential oscillation.

3.3 Tile current and voltage measurements

The PASTIS source by nature has an inherent systematic impedance. Using a set of Rogowski coils and capacitive voltage probes, we measure the tile currents and voltages respectively. Current and voltage probes are placed on/around the electrode shanks of tiles B1, B2, B3 and B4, between the backside of the chamber and the twisted pair connector as shown in figure 3.3. The current probes used were Bergoz CT-E1.0-S probes which are commercially available and have a 0.5V per Amp output signal with a 50Ω termination.

A number of voltage probe designs with direct connection to the tile shank were attempted. However, due to the high powers involved, many designs simply burnt out. As a result, in order to avoid direct thermal contact, the voltage probe design used is a capacitive probe. The design used a a capacitive-resistive

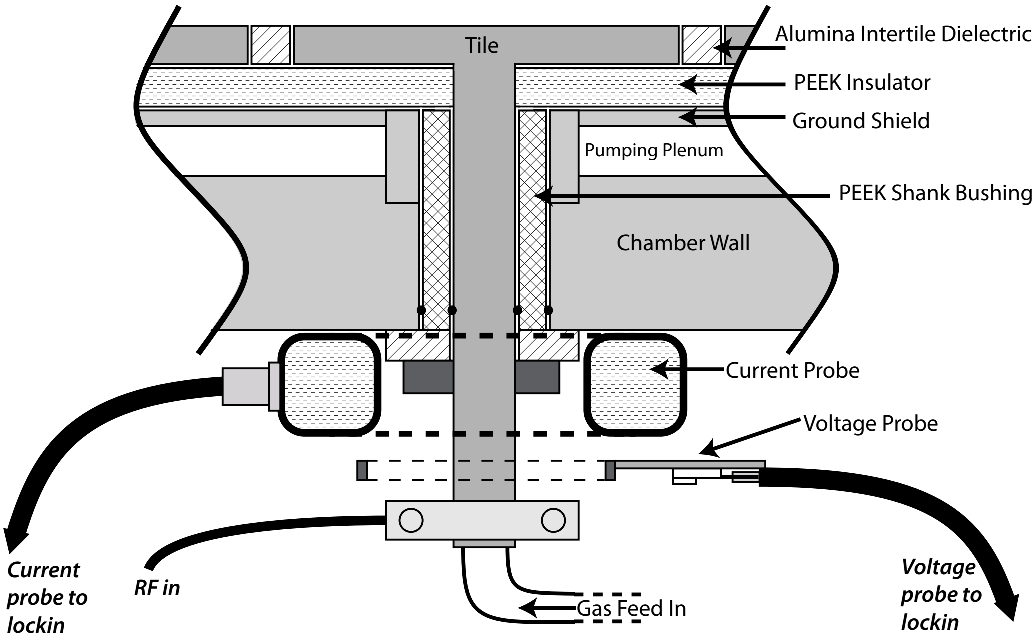

Figure 3.3: Showing the current and voltage probe mounted on the electrode shank on the backside of PASTIS

divider. The capacitor is formed from the 16mm diameter shank and a 2.5mm high × 40mm diameter copper ring. The resistive element is an ACT 50-Ohm, 20Watt ceramic-chip resistor.

The probe is constructed using a sheet of double-sided veroboard. A section of the top conductor and the insulator is cut away to expose the bottom conductor which acts as the ground reference for the probe. The 2.5mm ring is soldered to the top of the board and a 50Ω resister is soldered between the top and bottom conductors. A co-axial cable with the center conductor soldered to the top side of the probe and the outer conductor connected to the ground side of the resistor. The probe is grounded to the chamber mechanically by screwing it to a 40mm high aluminum block, which is attached to the backside of the chamber. Figure 3.4 shows a photo of a voltage probe similar to the one used and figure 3.5 shows an equivalent circuit diagram.

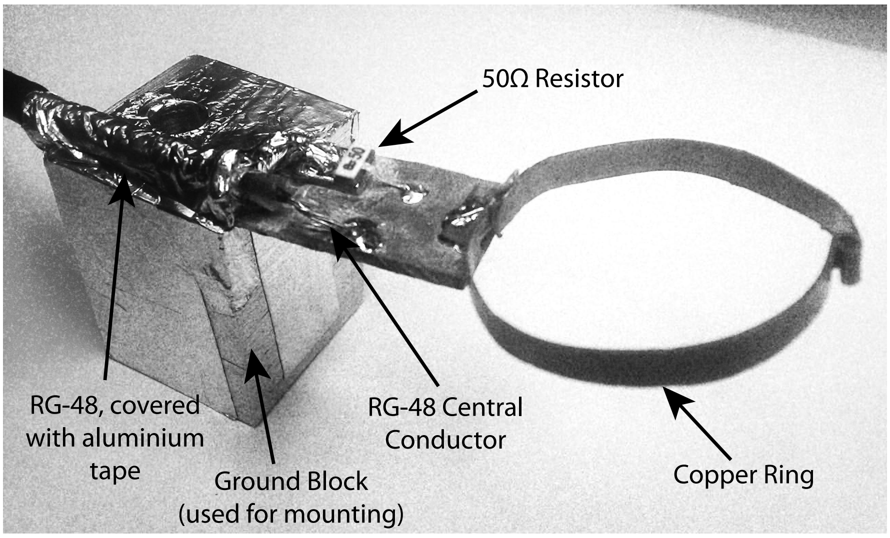

Figure 3.4: Photograph of a Voltage probe similar to the one used in this experiment

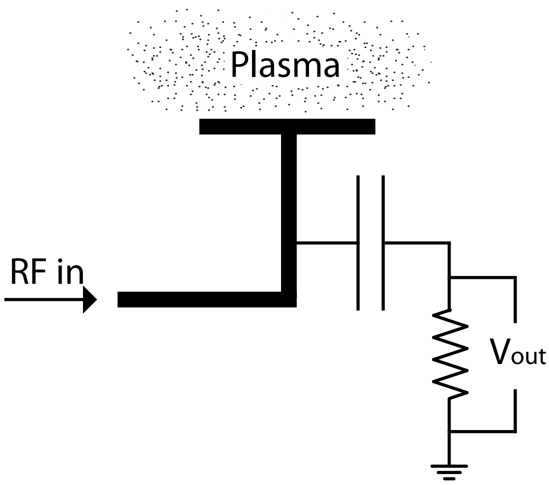

Figure 3.5: Equivalent Circuit diagram of Voltage probe

The probe response is determined for 150MHz using the capacitor equation.

$$C = \frac{\varepsilon_0 A}{d} \tag{3.3}$$

$$Z = \frac{1}{\omega C} \tag{3.4}$$

and is found to have an output

$$V_{out} = \frac{1}{40} V_{tile} \tag{3.5}$$

The amplitude and phase of both the tile current and voltage is measured using the SR-844 lock-in amplifiers and DAq board as described in section 2.5. A comparison between the PASTIS system in vacuum and plasma is made.

3.3.1 Current and Voltage measurements in Vacuum

When running in vacuum, there is no real part to the impedance between the tiles, i.e. purely capacitive coupling between tiles. The measured phase difference between current and voltage is defined as 90°. The system as a whole has resistance R_{sys}; this is dominated by the resistance of the wires in the PSTLD and transmission lines.

The amplitude of the measured signals is calculated as

$$A = \sqrt{X^2 + Y^2} \tag{3.6}$$

where $X = A.sin\theta$ and $Y = A.cos\theta$, the X and Y output DC signals from the $SR - 844$ lock-in amplifier [11]. The phase of both the current and voltage is calculated as,

$$\theta = tan^{-1}\left(\frac{X}{Y}\right) \tag{3.7}$$

This is the relative phase for vacuum.

We can calculate the magnitude of the impedance of the system from the amplitudes measured in vacuum using Ohm's Law,

$$P = I^2 R \tag{3.8}$$

therefore,

$$R_{sys} = \frac{P_{tile}}{I^2} \tag{3.9}$$

The total impedance of the load of the tiles and vacuum feedthru's can be calculated from

$$V = IZ = I[Re(Z) - Im(Z)] \tag{3.10}$$

with the real part known from equation 3.9.

3.3.2 Current and Voltage measurements with Plasma

The presence of plasma introduces an additional resistive load to the system. Again, the amplitude and phase of the currents and voltage is measured. The absolute phase shift between vacuum and plasma is calculated by subtracting the two values of phase from each other.

The addition of the plasma load adds a further component to the systematic impedance of PASTIS .

$$Z_{total} = Z_{sys} + Z_{plasma} \tag{3.11}$$

The sheath impedance of the plasma is calculated by subtracting the vacuum impedance Z_{sys} from the impedance measured with plasma.

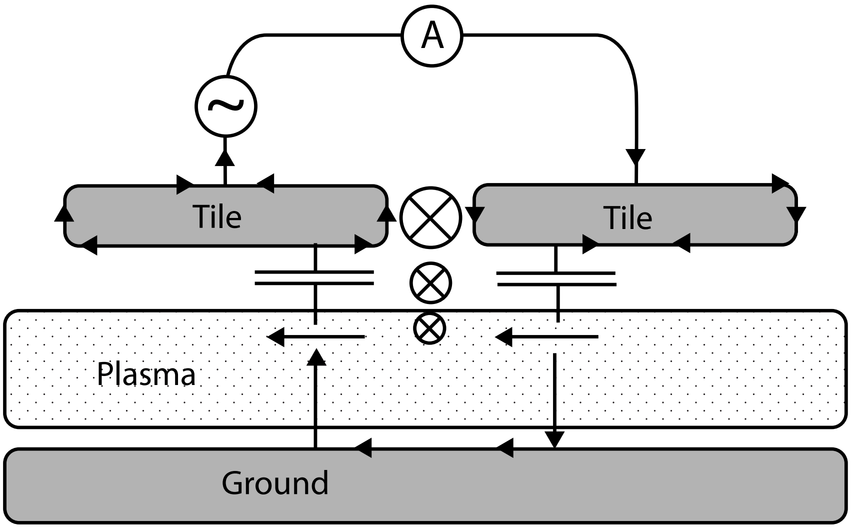

Figure 3.6: Showing the induced magnetic dipole between tiles

3.4 Magnetic flux probe

A current flowing in a loop induces a dipole moment, $\mathbf{m}$, the magnitude of which is defined by,

$$\mathbf{m} = I\mathbf{a} \tag{3.12}$$

where I is the current and $\mathbf{a}$ is the area vector. The direction of the dipole moment is given by the right-hand rule, (i.e., the direction the thumb of a right hand points if the fingers are pointing parallel to the current vector). The resulting magnetic vector potential, $\mathbf{A}_{dipole}$, as a function of distance r from the dipole is then,

$$\mathbf{A}_{dipole}\left(\mathbf{r}\right) = \frac{\mu_0}{4\pi}\frac{\mathbf{m} \times \vec{\mathbf{r}}}{r^2}, \tag{3.13}$$

where μ_0 is the magnetic permeability of free space [17].

In PASTIS , due to the push pull nature of the electrode array, surface currents in adjacent tiles cause a magnetic dipole to be formed between tiles (see figure 3.6). In vacuum, this dipole is due to the current flowing to bring the front side of the electrode to the electrode voltage and the current flowing to charge the capacitance between the tiles. Figure 3.6 shows the current paths that induces the magnetic dipole.

For example in vacuum the current flowing to the front of the electrode is small since

$$C = \frac{\epsilon_0 A}{d} = \frac{8.85 \times 10^{-12}(0.1^2)}{5.5 \times 10^{-2}} \tag{3.14}$$
$$\Rightarrow \frac{8.85pF}{5.5} \simeq 1.5pF \quad @ \quad 100V \tag{3.15}$$
$$\Rightarrow Z_{tile\,face} \approx 650\Omega \quad at \quad 150\,\mathrm{MHz} \tag{3.16}$$

While the current flowing to charge the inter-tile capacitance is comparitively large,

$$C = \frac{\epsilon_0 \epsilon_r A}{d} = \frac{8.85 \times 10^{-12} \times 10(0.1 \times 0.01)}{1.0 \times 10^{-2}} \tag{3.17}$$
$$8.85pF \Rightarrow Z_{tile\,edge} = 120\Omega \quad at \quad 150\,\mathrm{MHz}. \tag{3.18}$$

In plasma the capacitance of the sheath dominates. Thus more current must flow to the front side of the electrode to charge the capacitor.

$$C_{sheath} = \frac{\epsilon_0 \epsilon_r A}{d} \simeq \frac{8.85 \times 10^{-12} \times 1 \times (0.1^2)}{5.0 \times 10^{-4}} \tag{3.19}$$
$$885pF \Rightarrow \approx 1\Omega \quad at \quad 150\,\mathrm{MHz} \tag{3.20}$$

The impedance of the tile in plasma has a dependency on the the system capacitance *and* the sheath capacitance,

$$Im(Z) = \frac{1}{C_{Backside} + C_{Intertile} + C_{Sheath}}, \tag{3.21}$$

where $C_{Backside}$ is the capacitance between the backside of the tiles and the ground plate through the *PEEK* insulatator.

From equation 3.13, we expect the magnitude of the measured $\dot{B}$ signal to decrease with the square of the distance from the dipole. However in the presence of plasma, we expect the plasma to shield the measured magnetic flux, and thus expect the measured $\dot{B}$ signal as a function of position from the dipole to decrease faster than in vacuum.

3.4.1 Measuring the time-varying magnetic flux in PASTIS

A $\dot{B}$ probe works on the principle of a time varying magnetic field inducing a voltage in a conductive loop. From Faraday's laws, we know that this induced voltage across the terminals of the loop is proportional to the time rate of change in the magnetic field passing through the loop

$$V_{induced} = n.\vec{A}\frac{d\vec{B}}{dt}, \tag{3.22}$$

where n is the number of turns in the loop and $\vec{A}$ is a vector normal to the area enclosed by the loop with a magnitude equal to the area of enclosed by the loop.

A simple $\dot{B}$ probe consists of a loop of wire, which when inserted into an RF magnetic field produces a signal proportional to the magnetic field (equation 3.22). However $\dot{B}$ probes are susceptible to electrostatic pick-up along the length of the exposed probe [18, 19, 20], i.e. the time-varying electric fields within the plasma contribute to the signal produced by the probe. As a result, when operating in UHF/VHF conditions, capacitive pick-up of the common $\vec{E}$-field often dominates the the probe signal and the desired differential $\vec{B}$-field can be affected and/or lost.

Using a variety of techniques, a modified magnetic flux probe that separates the desired differential $\dot{B}$ signal from the electrostatic common-mode, is achieved.

The first such modification is to add electrostatic shielding to the body of

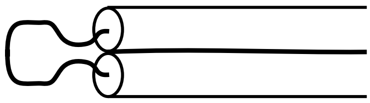

Figure 3.7: $\dot{B}$ probe loop with co-ax pair

the probe [19, 20]. This is achieved by using two lengths of RG-405 semi-rigid co-axial transmission line for the probe body. The two lengths of semi-rigid co-ax are soldered together along their entire length and from this point shall be referred to as a co-ax pair. (See figure 3.7.) This has a two-fold benefit. Firstly, capacitive pick-up between the probe and the plasma is reduced along the length of the probe body and secondly, it prevents cross-talk between the two channels of the transmission line.

The loop on the end of the co-ax pair is still exposed to electrostatic pick-up and despite the best efforts of all involved, the common-mode signal could not be fully eliminated. The solution is to add a co-axial transformer to the end of the co-ax pair [21]. A co-ax transformer is a well known device in *rf* impedance matching applications but here it is used to subtract the common **E-mode** pick-up from the raw probe signal, while adding the differential $\dot{B}$ signals together.

The implementation of the co-ax transformer also transforms the probe from a differential system to one that is single ended. The co-ax transformers used were made from the same co-axial transmission line as the co-ax pair and have a 2:1 ratio. The diameter of the loops ranges from 1.5cm to 6cm. The secondary winding/outer conductor is DC isolated from both the primary winding/inner conductor and the co-ax pair that is used for electrostatic shielding. A segment is removed from the outer conductor of the co-ax at the bottom of the loop nearest to the probe as illustrated in figure 3.8. The B-dot signal is acquired by measuring the voltage across the gap $A \rightarrow B$.

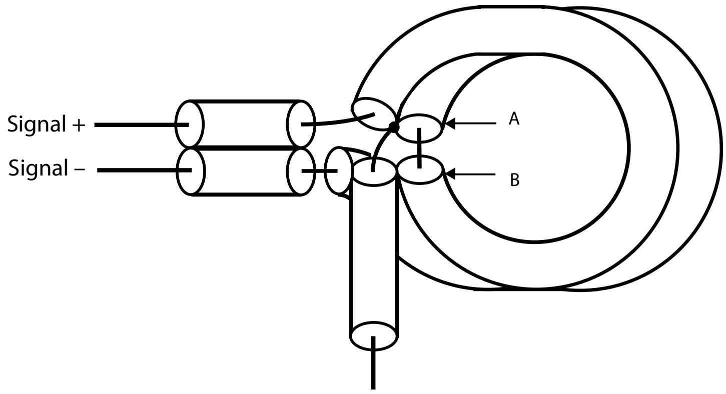

Figure 3.8: $\dot{B}$ probe loop with co-ax pair

3.4.2 *rf* grounding of the magnetic flux probe

The $\dot{B}$ probe is shown to work perfectly in a Helmholtz coil driven at low VHF power with a function generator. A clean 180° phase shift observed when rotating the probe through 180° . On PASTIS , however due to *rf* grounding issues it is difficult to obtain the correct signal.

To overcome this, the outer conductor of the co-ax pair and the single ended termination are both physically grounded to the outside of the chamber wall using a copper ground strap. When grounding the probe, care must be taken to ensure that no ground loops are possible and the potential of the probe with respect to ground is truly zero throughout the *rf* cycle

3.4.3 Electro-magnetic boundary conditions at the wall

Spatial measurements of induced magnetic dipole penetration into the plasma volume are performed by manipulating the $\dot{B}$ probe from the tile face through a vacuum feedthru in the ground plane facing the tile array until it is fully extracted from the plasma volume. The chamber wall opposite the tile array is made from

2cm thick aluminum and thus can be considered to be a "perfect conductor" (i.e. the conductivity $\sigma \to \infty$.) The electric field $\vec{E}$ in a perfect conductor is zero.

$$\vec{E} = 0 \tag{3.23}$$

The time-varying magnetic field in a loop L at the surface S is given by

$$\oint_L \vec{E}.d\mathbf{l} = -\frac{d}{dt}\int_S \vec{B}.d\mathbf{a} \tag{3.24}$$

According to electro-magnetic boundary conditions, the electric field parallel to the surface across a boundary is continuous, therefore the electric field in a lossy dielectric just outside the boundary also equals zero.

$$\vec{E}_{conductor} = \vec{E}_{dielectric} = 0 \tag{3.25}$$

So equation 3.24 becomes

$$\oint_L \vec{E}_{conductor}.\mathbf{l} - \vec{E}_{dielectric}.\mathbf{l} = -\frac{d}{dt}\int_S \vec{B}.d\mathbf{a} \tag{3.26}$$

$$-\frac{d}{dt}\int_S \vec{B}.d\mathbf{a} = -\int_S \dot{B}.d\mathbf{a} = 0 \tag{3.27}$$

Thus we see that the time-varying magnetic flux at the surface of a perfect conductor is zero [17, 22]. Thus when the probe is extracted from the plasma, to the position of the boundary, the magnitude of $\dot{B}$ should approach zero.

3.5 Ion Saturation Current Density

Chapter 1 considered currents collected by a biased 'electrode' placed in plasma. If the probe is sufficiently negatively biased, all electrons are repelled and only positively charged ions are incident on the probe tip. The time-averaged plasma

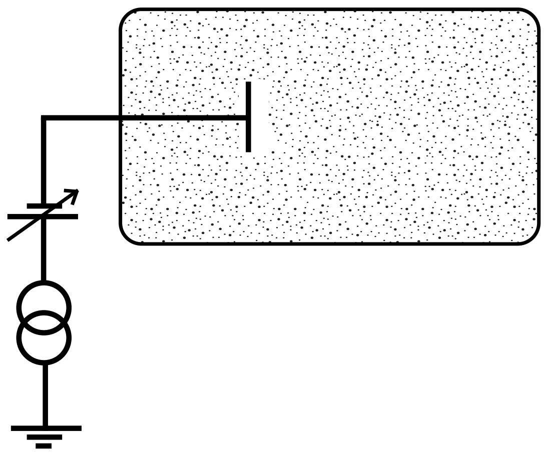

Figure 3.9: Planar Langmuir probe used to measure the ion saturation current density

potential has been previously measured to be approximately +18V[23]. As a result the probe is given a bias of -27V so that the electron current is suppressed.

$$I_e = I_{e,Sat} e^{\frac{-45}{2}} \simeq 0. \tag{3.28}$$

We calculate the magnitude of this current by measuring the voltage across a 10 kΩ resistor placed in series with the negative DC supply. An equivalent electrical diagram is shown in figure 3.9.

The probe tip is a flat circular tungsten disc that has a 4 mm diameter. It therefore has a charged collection area, A, of $1.25 \times 10^{-5}\text{m}^2$ or 0.125cm^2. (Sheath effects are ignored for simplicity)

By normalizing the ion suturation current obtained to the size of the probe tip we can define the plasma density at the sheath edge n_s as

$$J_i = \frac{e n_s u_B}{A} \tag{3.29}$$

where u_B is the Bohm velocity defined by,

$$u_B = \sqrt{\frac{kT_e}{m_i}}, \tag{3.30}$$

k is the Boltzman constant, T_e is the electron temperature and m_i is the ion mass. Here we assume that each ion is only singly ionized and the the electron temperature is a constant 2.2 eV.

The probe is inserted into the plasma through a vacuum feedthru and is manipulated along the long axis of the PASTIS chamber [16]. A DC-pass filter is connected in series with the circuit to ensure that no RF noise is collected and that only ion currents are measured. Plots of ion saturation current density are plotted as a function of spatial position in the chamber.

Chapter 4

Results

4.1 Capacitive Probe Measurements

Using a capacitive probe as described in section 3.2, the phase and amplitude of the plasma potential oscillation is analysed as a function of position in PASTIS. The probe is inserted into a re-entrant quartz tube which is immersed in the plasma and the probe is manipulated across the long axis of the chamber.

4.1.1 Spatial variation of the electric potential in vacuum

Figure 4.1 plots the phase and amplitude of the plasma potential oscillation of PASTIS. The top two traces (*a and b*) are the phase (relative to the current on tile B1) and amplitude in vacuum. The bottom two traces are the relative phase and amplitude in a diffuse plasma at 50W. Note the position of the four tiles shown along the *x-axis*. Figure 4.1 (a) shows that there is a 180° phase shift observed between adjacent tiles and that the transition between the phases at the tile boundary is sharp.

The amplitude of the plasma oscillation potential in vacuum is near constant across the tile face and is zero at the tile boundary. Furthermore the amplitude measured in front of paired tiles is equal. There is a difference between pairs but this is likely due to the coupling efficiency of the loop in the PSTLD power splitting device.

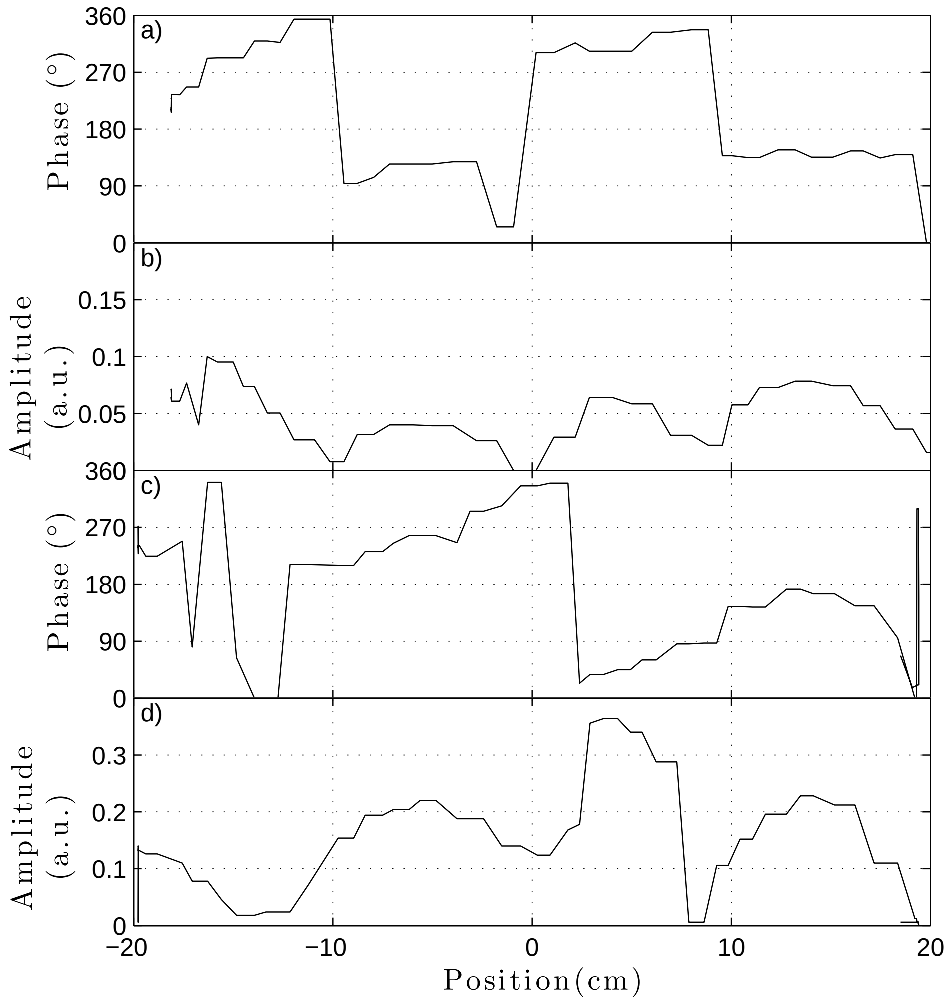

Figure 4.1: Plot of *rf* spatial potential oscillation versus position in vacuum (*a & b*) and plasma potential oscillation at 50W (*c & d*). Spatial structure of the respective phases, *a* and *c* and the amplitudes *b* and *d* can be seen.

4.1.2 Spatial profiles of the plasma potential oscillation

The spatial structure imposed by the tile array is still evident in low power plasma. In figure 4.1 (d), it can be seen that the amplitude of the fundamental frequency of the plasma potential oscillation has four distinct peaks that correspond to the tile array.

The phase in plasma is more complicated, however. While there is still a ~180° phase shift between tiles, the transition between phases is no longer a sharp transition as seen in vacuum. It is, rather, a smoother change that takes place over a distance wider than the thickness of the inter-tile gap, (i.e. > a few centimeters). This is seen in figure 4.1 (c).

As power is increased, the length that this smoothing of phases becomes longer than the width of the tiles. As a result the 180° shift between adjacent tiles is often no longer obvious.

Further increases in power give rise to an asymmetrical spatial profile in the measured plasma potential oscillation. The reasons for such a profile remain unclear, however an effort to describe its origin is attempted in Appendix A.

4.2 Current and voltage measurements

4.2.1 Amplitude of Current and Voltage

Figure 4.2 shows a plot of current and voltage as a function of power for the PASTIS source operating in vacuum. There is a linear relationship between current squared and power. From Ohm's law,

$$P = I^2 R_{sys}, \tag{4.1}$$

we can deduce that R_{sys}, the resistance of the system, is constant in vacuum. The series resistance of PASTIS in vacuum is calculated to be $\approx 1\,\Omega$. Note too that the voltage also scales with the square root of power in vacuum.

The introduction of plasma to the system adds an additional load in series with the capacitive impedance of the plasma. In figure 4.3, plots of the amplitude and phase of

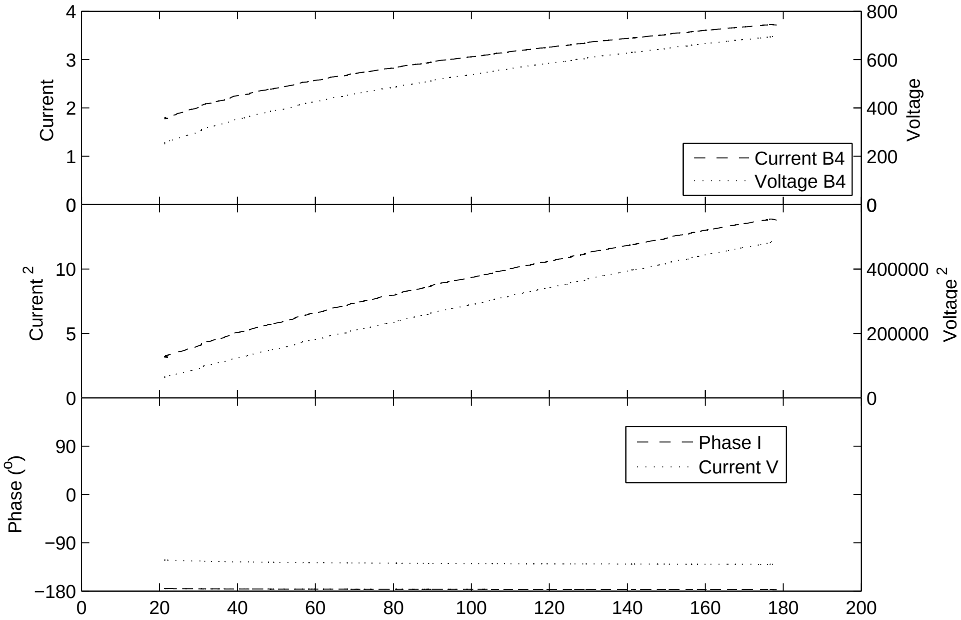

Figure 4.2: Plot of current and voltage as a function of power in vacuum

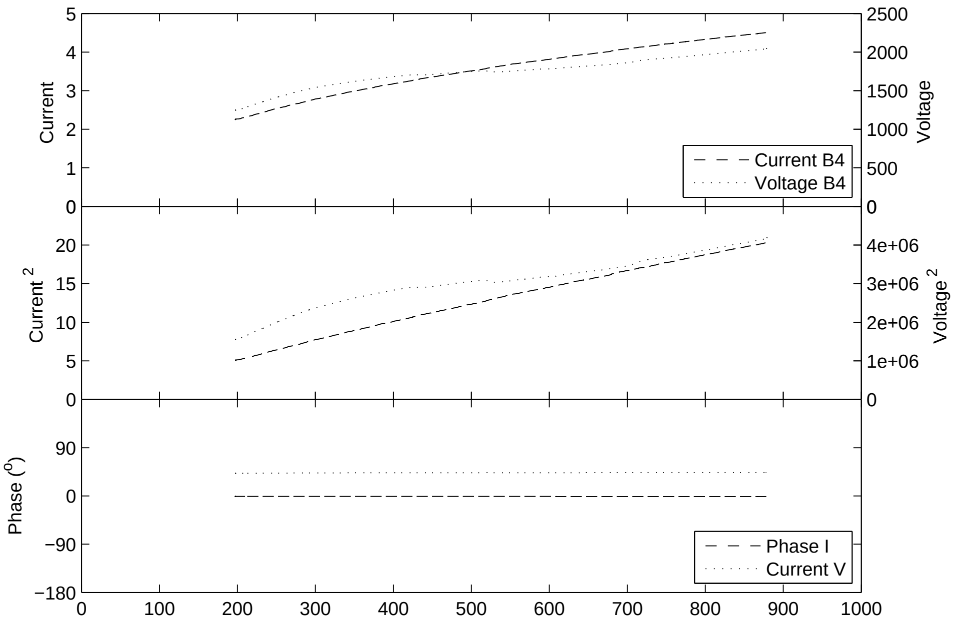

Figure 4.3: Plot of current and voltage as a function of power in an Argon plasma at 50 mTorr .

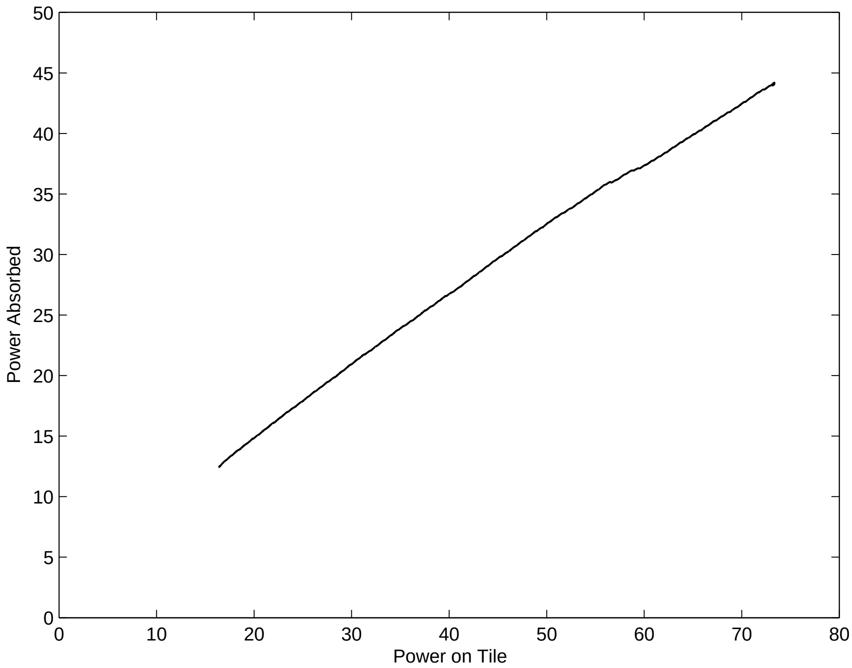

Figure 4.4: Plot of power absorbed by the plasma as a function of *rf* power

the current and voltage versus power are presented in plasma at 50 mTorr .

The current flowing between tiles is reduced by approximately a factor of two, while the measured voltage is nearly doubled for the same power.

Once again, the current squared scales almost linearly with *rf* power. The slight increase in the slope is thought to be due to a reduction of the capacitive impedance of the sheath at higher power. The power absorbed by the plasma is calculated by:

$$P_{plasma} = P_{rf} - I^2 Z_{sys} \tag{4.2}$$

A plot of power dissipated power versus *rf* power on tile B1 is shown in figure 4.4. There is a near linear relationship between the power applied to the tile and the power absorbed by the plasma.

Analysis of the voltage with respect to power, however, reveals a non-linear relationship between the voltage and power. At low power (<300W), the voltage is proportional to the square root of power. This suggests that the impedance of the plasma at lower powers is constant. As power is increased, the rate of change of voltage with respect to power is reduced, indicating a change to a power coupling mode that is both capacitive and inductive.

4.2.2 Phase of Current and Voltage

Examining the phase difference, between current and voltage in vacuum in figure 4.2, we see that there is a small ($\sim 10°$) drift in the phase of both current and voltage. It is thought that this in part due to the lock-in reference signal being taken from the azimuthal field in the match-box. As the reflected power drifts with increasing forward power, so too does the phase of the azimuthal magnetic field within the matchbox.

Because the current coupling in PASTIS is assumed to be purely capacitive, the phase of the current is thus defined as 90° ahead of the phase of the voltage. The measured phase difference is corrected to reflect this.

In plasma, there is approximately a 180° shift in the measured phase of both the current and voltage as seen in figure 4.3. Once again this is due to the location of the lock-in reference signal being placed in the matchbox because the change in tile load-impedance results in a different standing wave pattern along the twisted pair (transmission line) between the output of the PSTLD and the tiles. The different "tuned" position of the capacitors in the matchbox affects the phase of the azimuthal magnetic field within the transmission line.

The absolute difference in phase between the current and voltage is more important however. Thus the same correction factor is applied to the phase between current and voltage and a comparison between the phase difference in vacuum is made.

With plasma the capacitance of the tiles increases, reducing the reactive impedance; inductive power coupling would also serve to reduce the inductance of the system, which would also serve to decrease the load reactance, as it remains dominated by the capacitive load.

4.2.3 Plasma Impedance

Knowing the phase and magnitude of the impedance, information on the magnitude of the real and imaginary elements can be obtained. The real element of the impedance, Z_{Re}, is obtained from

$$P = I^2 Z_{Re} \tag{4.3}$$

where P and I are the calculated power and measured current at each tile respectively. The total impedance Z is calculated from Ohm's law as the ratio of the measured voltage and current

$$\begin{aligned} V &= IZ & (4.4) \\ \Rightarrow Z &= \frac{V}{I} & (4.5) \end{aligned}$$

From the total and real element of the impedance, the imaginary component is established from

$$Z_{Im} = \sqrt{Z^2 - Z_{Re}^2} \tag{4.6}$$

A plot of the real and imaginary components of the impedance as a function of *rf* power in both vacuum and plasma is shown in figure 4.6.

In vacuum, both the real and imaginary impedances increase with increasing *rf* power. In plasma we see that the real impedance increases with increasing *rf* power; the resistivity of the plasma increases with plasma density. The imaginary component of the impedance decreases indicating that the capacitance of the sheath is increasing with *rf* power. Capacitive impedance (Z_C) is inversely proportional to capacitance.

$$Z_C = \frac{1}{j\omega C} = \frac{-j}{\omega C} \tag{4.7}$$

Current and voltage probe measurements are taken at a point on the electrode shank as depicted in figure 3.3. As a result there is a finite electrical path length between the plane of measurement and the plasma load. The presence of plasma further increases

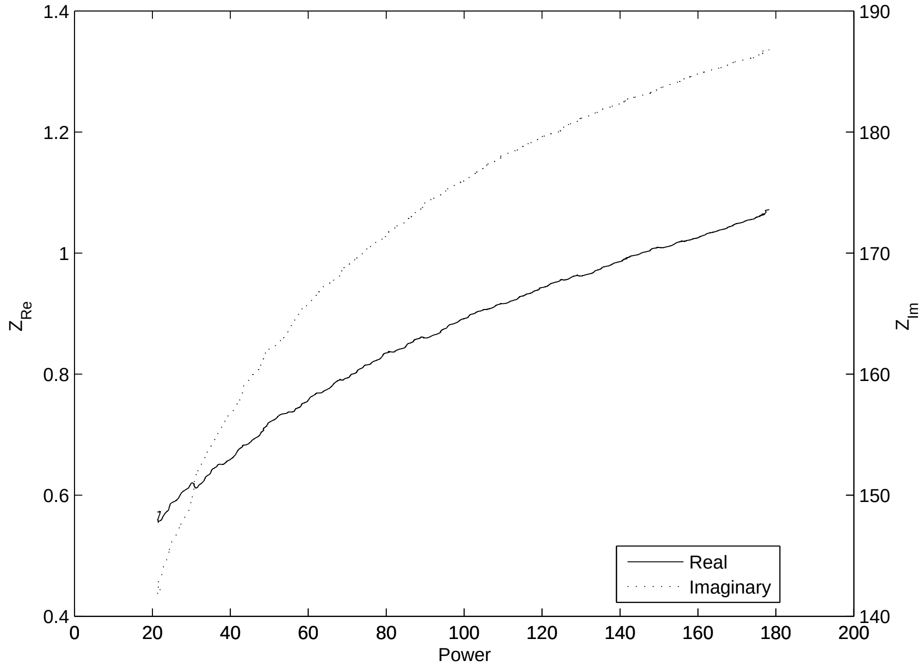

Figure 4.5: Plot of the real and imaginary components of the impedance as a function of *rf* power in vacuum

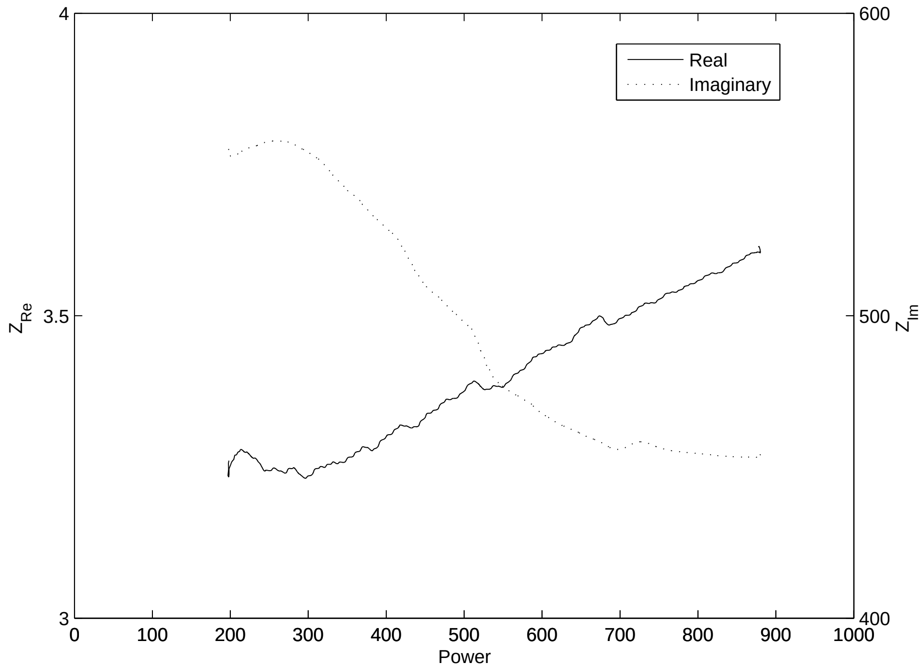

Figure 4.6: Plot of the real and imaginary components of the impedance as a function of *rf* power in plasma

this electrical path meaning that a comparison of the real and imaginary impedances in vacuum and plasma is non-trivial. A description of framework required to establish a consistent model is outlined in Appendix B.

4.3 Magnetic Flux Probe Measurements

The time varying magnetic flux is measured as a function of both power and position relative to the source using a $\dot{B}$ probe as described in section 3.4. Using MATLAB, the measured magnetic flux is plotted as a function of position and power.

Figure 4.7 plots $\dot{B}$ data versus position in vacuum at 100W and in a low-power plasma state (100mTorr Argon @ 300W). The top graph is the measured $\dot{B}$ amplitude, the middle graph is $\dot{B}$ amplitude normalized to the tile current, and the bottom graph is the $\dot{B}$ relative phase to the phase reference.

4.3.1 Time-varying magnetic flux analysis in PASTIS in Vacuum

Upon first inspection of the system in vacuum, we find that there is a large time-varying magnetic flux close to the tiles, due to the dipole moment induced between tiles. In vacuum, the measured time varying magnetic flux decreases monotonically with distance from the plane of the tiles.

A number of effects have been identified which contribute to the shape of the profile. The dominating effect is that of near-field dipole radiation, which scales with $1/\left(\frac{r}{d}\right)^2$, where r is the distance from the dipole with a characteristic length, d.

Other effects which contribute to the shape of the profile are the ground plane, 5.5cm away from the tile array. Boundary conditions for a conductive surface dictate that the magnetic flux parallel to the boundary at the surface must equal zero.

$$\dot{B}_{\|,surface} = 0 \tag{4.8}$$

In addition to this, the neighboring dipole fields from adjacent tile boundaries are 180° out of phase. Thus there is a small far field dipole radiation ($\propto 1/\frac{r}{d}^3$).

As the probe reaches the edge of the plasma volume, (a point 5.5cm away from the surface of the electrode) the measured magnetic flux has reached zero. This is consistent with the boundary conditions, that the time-varying magnetic flux is zero in a conductor. We note also that the phase is constant throughout the scan.

4.3.2 Time-varying magnetic flux analysis in PASTIS in the presence of Plasma

In the presence of plasma, the profile of the induced probe voltage is observed to be vastly different to that in vacuum. In low power plasma, 300W, (figure 4.7) we see that the magnetic field initially decreases with increasing distance from the tiles. However as plasma currents begin to dominate, an increase in magnetic flux is observed.

Figure 4.8 shows $\dot{B}$ profiles at selected powers. As power increases, 500W we see that the increased plasmas density shields the currents within the plasma therefore reducing any magnetic fields present in the plasma. This effect is shown in figure 4.8. We also observe that further increases in power (and therefore the plasma density) do not change the shape of the acquired graph

It was expected that in the presence of plasma, there would be a faster decay of the measured magnetic flux as a function of increasing distance from the electrode due to plasma shielding effects. However, this is inconsistent with the experimental results.

As can be seen in figures 4.7 and 4.8 the characteristic length of the decay in plasma is actually longer than in vacuum. Reevaluating the model, it was determined that in vacuum, little or no current flows across the face of the tile, i.e. current flows capacitively between tiles only through the adjacent tile edges. Thus the characteristic length of the dipole is dominated by the gap between tiles. In addition to this, the alumina inter-tile dielectric has a high k, thereby further facilitating the flow of capacitive current between tiles.

In plasma however, the thin plasma sheaths promote the flow of current across the

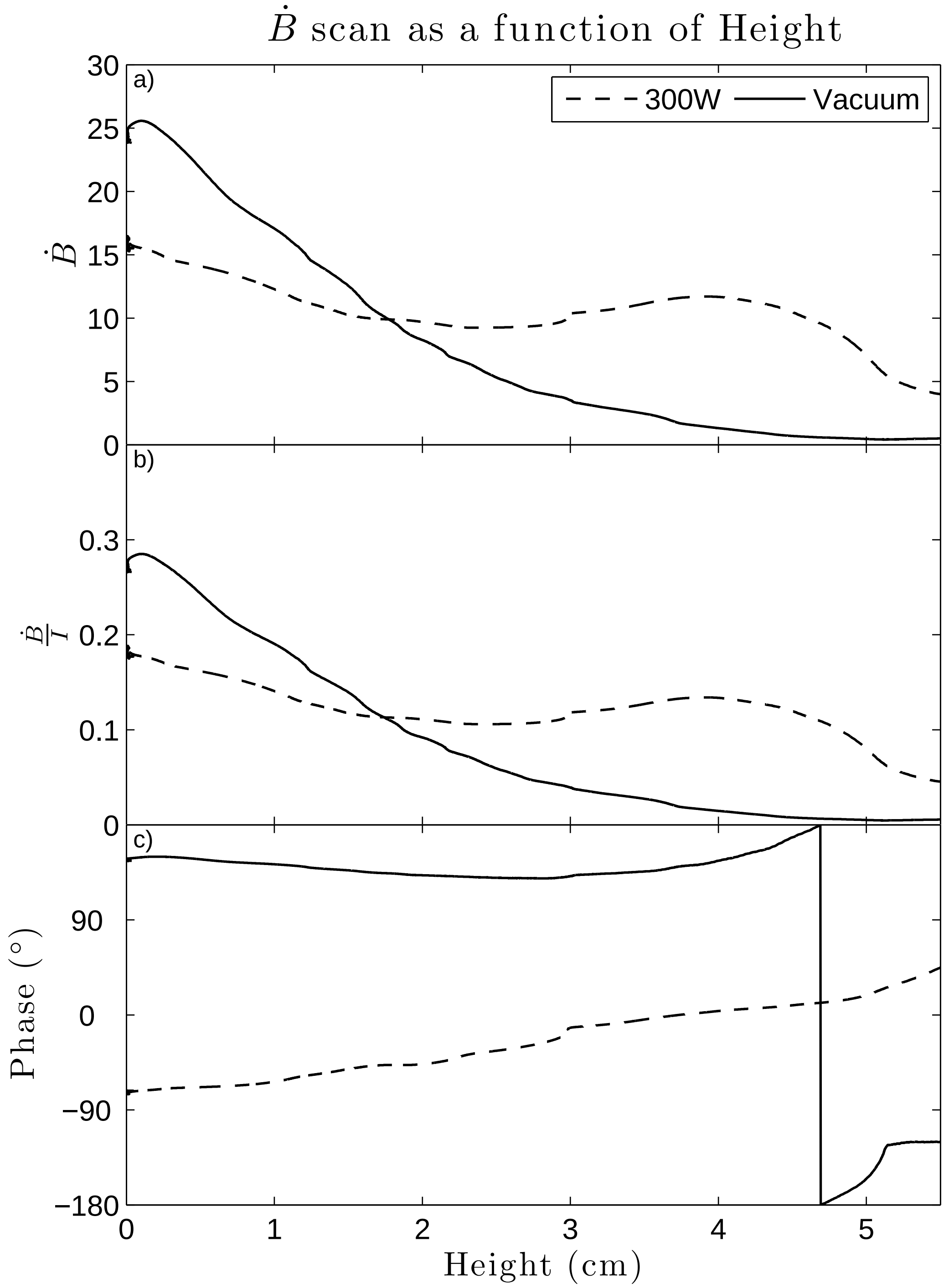

Figure 4.7: Plot of induced $\dot{B}$ voltage as a function of distance from electrode in vacuum and plasma at 300W

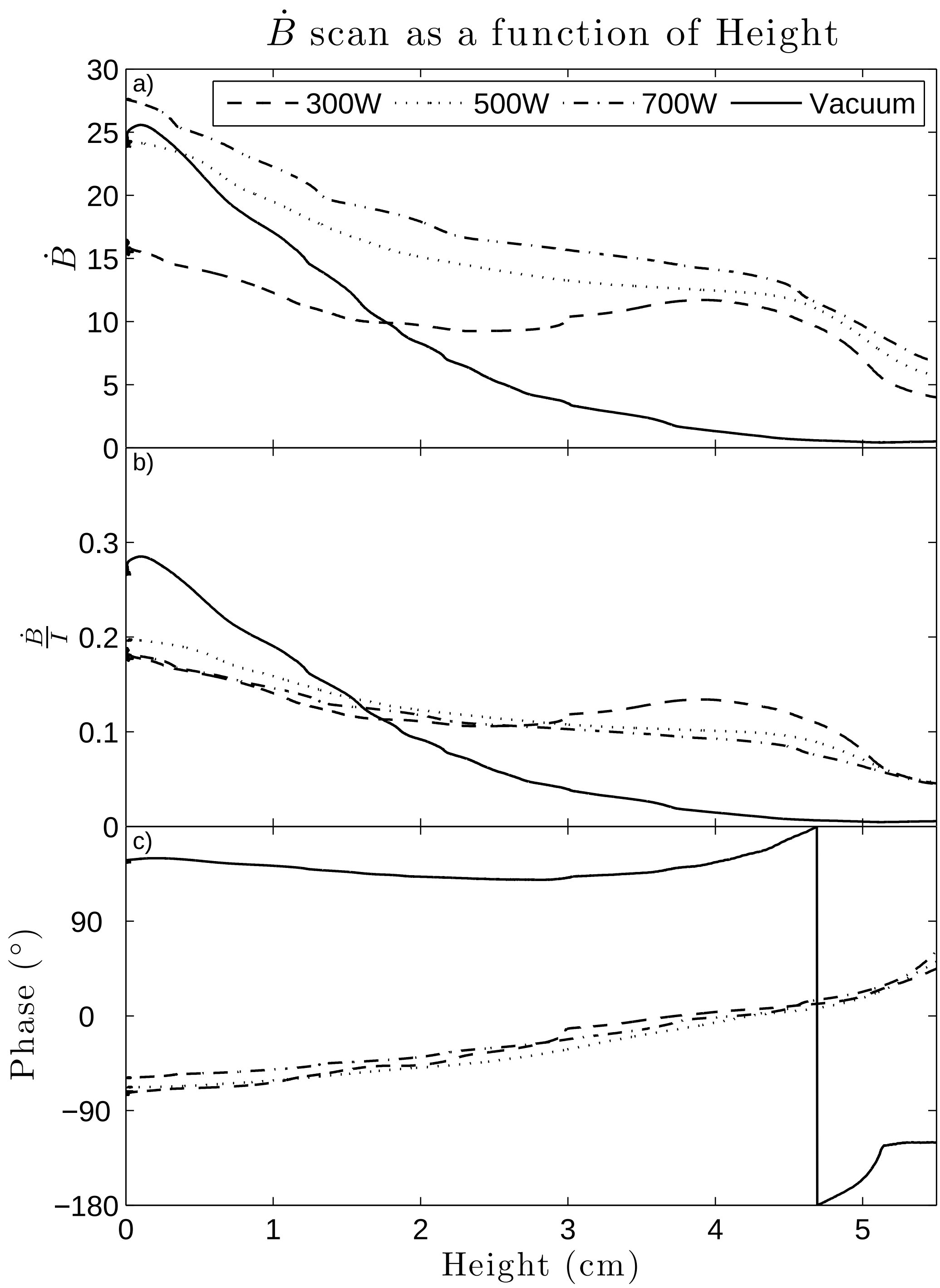

Figure 4.8: Plot of induced $\dot{B}$ voltage as a function of distance from electrode in vacuum and plasma for a 300, 500 and 700W

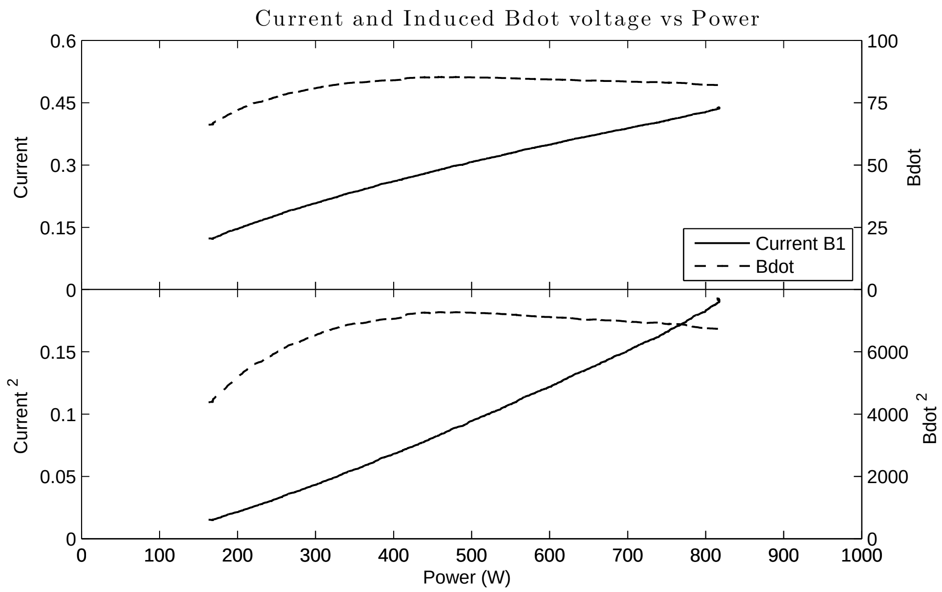

Figure 4.9: Plot of induced $\dot{B}$ voltage and tile current vs Power

face of the electrode exposed to the plasma. As a result, the effective length of the magnetic dipole is longer.

For all Z-scans in plasma, we see that there is a constant phase shift in the $\dot{B}$ signal. When the probe is fully removed from the plasma volume, we see that the phase is close to that of the phase for the system in vacuum

In order to allow a direct comparison between Z-scans at different powers, the acquired profiles are normalized to the tile current.

4.3.3 Power ramping

Figure 4.9 plots the time varying magnetic flux and current as a function of *rf* power 15mm away from the tiles array. The top graph is a plot of the measured $\dot{B}$ and current as a function of power. The bottom graph is a plot of the $\dot{B}$ squared and current squared versus power.

At lower powers, the induced $\dot{B}$ voltage and the antenna current scale with the square root of power. As power is increased, rate of change of the measured $\dot{B}$ signal decreases. A further increase in power yields a peak and a slight drop in $\dot{B}$ signal as plasma effects shield the probe loop from magnetic fields.

4.4 Langmuir Probe

Spatial scans of electron density are performed by manipulating a planar Langmuir probe across the long axis of PASTIS . Ion saturation current density is measured as a function of position. By assuming that the electron temperature, T_e is spatially constant, the plasma density at the sheath edge is measured by

$$J_i = \frac{e n_s u_B}{A} \tag{4.9}$$

where u_B is the Bohm velocity

$$u_B = \sqrt{\frac{kT_e}{m_i}}. \tag{4.10}$$

rearranging equation 4.9 and subbing in 4.10, the electron density at the sheath edge is therefore found using,

$$n_s = \frac{J_i A}{e}\sqrt{\frac{m_i}{kT_e}}. \tag{4.11}$$

4.4.1 Ion Saturation Current Density measurements

Figure 4.10 shows a plot of ion saturation current density as function of probe position in PASTIS for a range of powers at 400 mTorr . From the data, it is clear that there is a definite spatial structure in the electron density of plasmas produced in PASTIS. Closer inspection reveals that this spatial structure is aligned with the array of tiles that make up the segmented electrode. In front of the tile boundary there is a local maximum in the measured ion saturation current density. Conversely there is a local minimum in front of the centers of the tiles. This corresponds to a local maximum and local minimum in the plasma density respectively.

4.4.2 Power Dependance

In figure 4.10 we see that as power increases, so too does the measured ion saturation current density. However at low power (<400W) there is little coupling to the edge of the chamber, while at high power, the ion saturation current density is observed to be

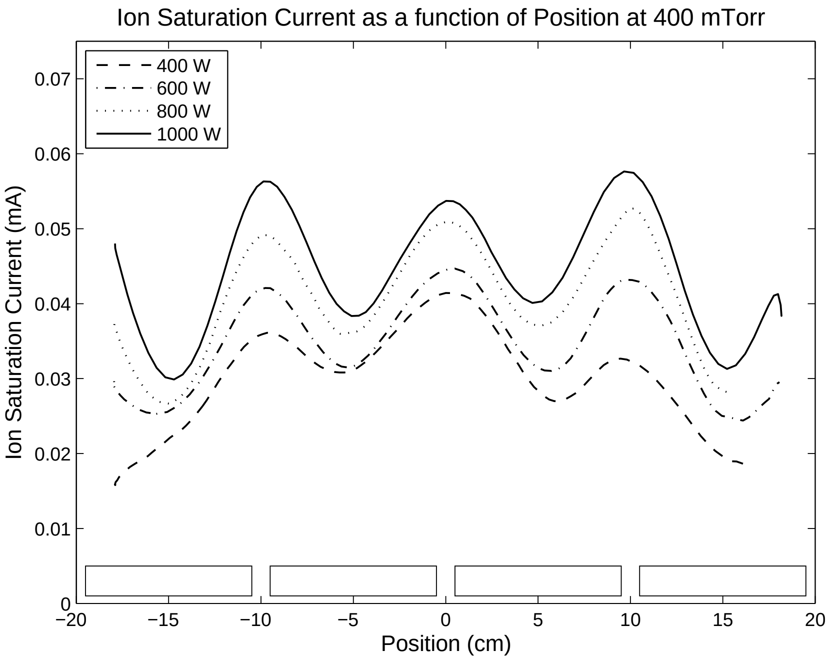

Figure 4.10: Plot of ion saturation current density versus probe position for a range of powers at 400mTorr

comparable to the inter-tile peaks. This indicates that there is coupling through the ground plane outside the edge electrodes.

The relative height of the inter-tile peaks changes with respect to power too. At lower powers, the center peak, over the B2/B3 boundary, is larger than peaks observed at the B1/B2 and B3/B4 boundaries. However as power increases, the height of the outer pairs (B1/B2 & B3/B4) increase relative to the height of the center tiles (B2/B3). This supports a model of increased edge coupling mentioned above.

The spatial profile of the ion saturation current remains at different pressures as seen in figure 4.11, a plot of the ion saturation current density versus position at 200mTorr. Comparison of the measured ion saturation density normalized to power at 200 mTorr is approximately a factor of two larger than at 400mTorr.

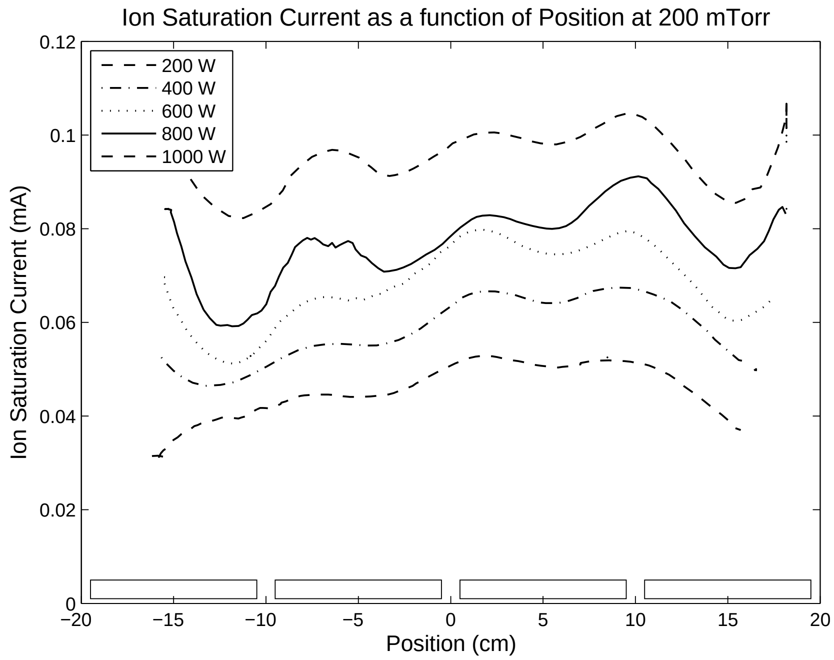

Figure 4.11: Plot of ion saturation current density versus probe position for a range of powers at 200 mTorr

4.4.3 Pressure Dependance

Figure 4.12, shows a plot of ion saturation current vs position at a fixed power for a number of differing pressures. We see that the average ion saturation current density increases with decreasing pressure. This is due to higher energy losses per electron-ion pair produced at lower electron temperatures as described by Gudmundson 2000 [24, 25, 2]. Changing the neutral density causes the electron temperature to decrease as determined by power and particle balance in a global model [2]

In addition to this, ratio of the relative heights between the local maxima and minima is smaller, indicating a plasma that is spatially more homogeneous. The mean free path, λ of a gas is inversely proportional to its density, n_g,

$$\lambda = \frac{1}{n_g \sigma} \tag{4.12}$$

where σ is the collisional cross section of the species, meaning that at lower pressures,

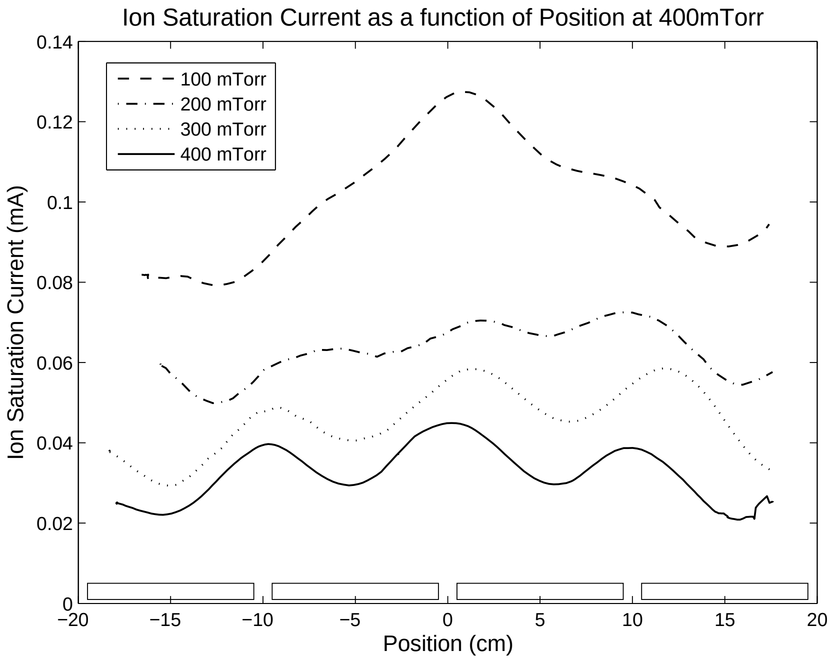

Figure 4.12: Plot of ion saturation current density versus probe position for a range of pressures at 500Watts

there is more diffusion of species (electrons, ions and neutrals) throughout the plasma volume.

Chapter 5

Analysis of Data

In Chapter 4 a description of the results of the various spatial experiments is provided. Using what has been learned from these results, an interpretation of the relationship between the data is presented here.

Langmuir probe profiles of the ion saturation current density in PASTIS show that there is a well defined spatial structure imposed on the plasma in a multi-tile source. Spatial profiles of the ion saturation current density are obtained and assuming a spatially constant electron temperature, the plasma density is calculated.

Results of Langmuir probe measurements point to a higher plasma density in the area in front of the tile boundary. We have identified two factors which could promote increased ionization at the tile boundary.

The first such is the presence of the induced time-varying magnetic field adjacent to the plasma volume. Because PASTIS is powered in the VHF range, there is a low electrical skin depth and currents flow near the surface of conductors. In addition to this reduced skin depth, and the push pull nature of PASTIS , a magnetic dipole is formed between the tiles. This magnetic dipole is measured with a magnetic flux probe.

In vacuum, the amplitude of this dipole is found to decay with increasing distance from the tile boundary. The length of this decay is determined by the characteristic length of the dipole. In vacuum, very little current flows along the tile surface that faces the plasma volume. As a result, the effective length of the dipole can be approximated to be the distance between the tiles.

In plasma, the conductivity of the plasma volume enables current to flow around the entire surface of the tile. Thus the effective characteristic length of the dipole is longer and it penetrates further into the plasma. This is seen in the data as the length of the decay of the amplitude of the measured dipole is now longer than the thickness of the plasma volume.

However, the characteristic decay length of the induced magnetic dipole does not scale with power, suggesting that the peaks in ion saturation density are not caused by the induced time-varying magnetic field adjacent to the plasma volume.

Capacitive probe measurements also show a definite spatial structure imposed on the electric potential in PASTIS . In vacuum, we see that this spatial structure is a direct result of the multi-tile nature of PASTIS . Four wide peaks are observed to coincide with the structure of the tile array. There is a 180° shift in the measured phase of the electric potential as the capacitive probe tip is manipulated across the tile boundary. This change in phase takes place very quickly, over the length of the 1cm inter-tile dielectric.

In the presence of plasma, the four peaks corresponding to the amplitude of the measured plasma potential oscillation are still prominent in the spatial profile. However it is observed that distance over which this transition between phases takes place is broadened. This is due to plasma shielding of the localized electric field and the conductivity of the plasma smoothing local perturbations.

The peaks between tiles are a result of the tiles being driven 180° out of phase, giving rise to a large potential difference across the tile boundary and a larger plasma potential oscillation. An increased spatial potential difference will result in a higher rate of localized ionization thus giving a higher ion density at the tile boundary.

The spatial profiles of the ion saturation current density also exhibit a pressure dependence. Lower pressure plasmas tend to be more homogeneous i.e. have less spatial structure. This is because mean free path of the species in the plasma is increased at lower pressure. Furthermore, the average value for the ion saturation current density is higher at lower pressure. This is the result of a two fold effect; firstly, the electron temperature is lower at lower pressures and secondly, the ionization cross section is reduced at lower electron temperatures.

Current and voltage measurements show that when operating in vacuum, the PASTIS plasma source has a constant resistance and obeys Ohm's law, i.e. $V = IR$. PASTIS is a capacitively couple discharge source and so the current and voltage are 90° out of phase.

The introduction of plasma adds a further capacitive and inductive load in series with the capacitive impedance of the system in vacuum. As a result, current and voltage measurements are no longer proportional to the input *rf* power.

The current in particular is now "sublinear" when plotted as a function of the square root of the *rf* power.

By analyzing the current and voltage measurements in plasma, the response of the impedance of the plasma with respect to power is revealed. It is found that both the real and imaginary elements of the impedance reduce with increasing *rf* power. This suggests that the conductivity of the plasma is increasing and the resistivity of the sheath is decreasing with increasing power.

Further analysis of the current and voltage data, indicate that the power absorbed by the plasma is almost linearly proportional to the input *rf* power.

Chapter 6

Discussion & Conclusions

A scalable multi-tile electrode plasma source operating in a VHF regime has been described and an investigation of the spatial structure of plasmas properties in the source has been reported.

The properties investigated are: impedance of the plasma in front of individual tiles in the segmented electrode-tile array; spatial profiles of the ion saturation current density across the long axis of the source -parallel to the plane of the electrode array; spatial profiles of the fundamental harmonic of the plasma potential oscillation at the *rf* drive frequency in the plane of the electrode array and penetration of induced *rf* magnetic fields into the plasma as a function of distance from the plane of the electrode - perpendicular to the electrode array.

Four different plasma diagnostics are applied to examine these properties; they are time-varying magnetic flux probe measurements of the magnetic flux, planar Langmuir probe measurements of the ion saturation current density, capacitive probe measurements of the plasma oscillation potential and analysis of the tile current and tile voltage to investigate the impedance of the PASTIS source with and without plasma.

The plasma potential oscillation, as measured with a capacitive probe, has a spatial structure imposed by the tile array. A spatial profile with four peaks corresponding to the tile array with a 180° phase shift between tiles is observed in vacuum. However, in the presence of plasma, while the four peaks are still present above the tiles, it is observed that distance over which the transition between phases takes place is broadened. This is due to plasma shielding of the localized electric field and the conductivity of the plasma smoothing local perturbations.

The PASTIS source has an impedance that is constant with respect to the the applied *rf* power. The impedance of plasmas produced by PASTIS (which add a load in series with the antenna array), however changes with power as the conductivity of the plasma and the impedance of the sheath change as the plasma becomes more ionized and absorbs more power.

Because of the VHF frequencies being used in PASTIS , there is a small skin depth in the electrical conductors, and thus only surface currents flow through the conductors in the powered electrode/tile array. Consequently differential currents on neighboring tiles result in *rf* magnetic fields being imposed on the plasma. A time-varying magnetic flux probe is used to measure magnitude and phase of induced dipole moment and how far it penetrates into plasma volume in vacuum and with plasma. The presence of plasma determines the capacitive impedance of the system and the characteristic length of this induced dipole thus how far it penetrates into the plasma volume. Contrary to the predicted model, results show that in plasma, the characteristic length of the dipole radiation is largely unaffected by power or plasma density, indicating that plasma in front of the tile boundary is not inductively coupled.

The large potential difference between tiles measured with the capacitance probe results in higher plasma density in front of the tile boundaries. Using a Langmuir probe, the ion saturation current density is measured as a function of spatial position. By assuming a constant electron temperature throughout the chamber, the ion saturation current density of the plasma is calculated confirming a higher plasma density in front of the tile boundaries.

Appendix A

Asymmetric spatial profiles of plasma potential oscillation

As described in section 4.1, the spatial variation of the plasma oscillation potential at higher powers has an asymmetric profile that contradicts the current model. Figure 4.1 shows the spatial profile in both vacuum and low power plasma. Four peaks corresponding to the four powered tiles of the electrode with a 180° phase shift between each tile are observed as expected.

However, when the power is increased, the expected profile does not behave accordingly. At higher powers, the spatial profile has two peaks with a wide trough in between. The location of the peak does not coincide with the tile array but instead with the location of the *ISO-100* view ports on PASTIS . There is a peak over tile B2 which is in between two windows. The other peak is between the edge of the plasma volume and the window near C4.

The capacitance in front of the windows should be lower and thus the capacitive impedance should be higher as

$$Z = \frac{1}{\omega C}. \tag{A.1}$$

According to theory, the measured potential should be higher in front of the windows as the ratio of the impedances of the potential divider (the probe tip) is higher here.

However the observed spatial profiles of the plasma potential oscillation show the opposite. As a result a different model needs to be considered.

It is possible that the probe is subject to *rf* interference. The length of the probe is 1080mm which is a significant fraction of the driving *rf* wavelength. Furthermore if the second conductor of the tri-ax is allowed to oscillate, (the 10mm before the probe tip and the last 150mm do not have the outer tri-axial shield), could drive current across the $50\,\Omega$ resistor thus giving misleading values and results

Appendix B

On the analysis of the impedance in plasma and vacuum

In Chapter 4, comparison of the measured impedance of the tiles in vacuum to that in plasma shows that, contrary to the anticipated model, there is an increase in the total impedance in the presence of plasma. The current flowing between tiles with plasma is reduced by approximately a factor of two, while the measured voltage is nearly doubled for the same power.

It would normally be expected that the impedance of an open circuit (running in vacuum) is significantly greater than that of a resistive circuit (running with plasma).

$$Z_{open} \gg Z_{resistive} \tag{B.1}$$

An attempt to describe the potential origin of this inconsistency is outlined here.

Recall that in Chapter 3, the measurement of the current and voltage is acquired using probes mounted on the electrode shank as depicted in figure B.1. As a result of being mounted on the electrode shank, there is a finite electrical path length between the plane of measurement and the plasma facing tile surface.

Let us consider first the system operating in vacuum and assume that a purely open circuit exists at the plasma facing tile surface. There is a short circuit in the coupling

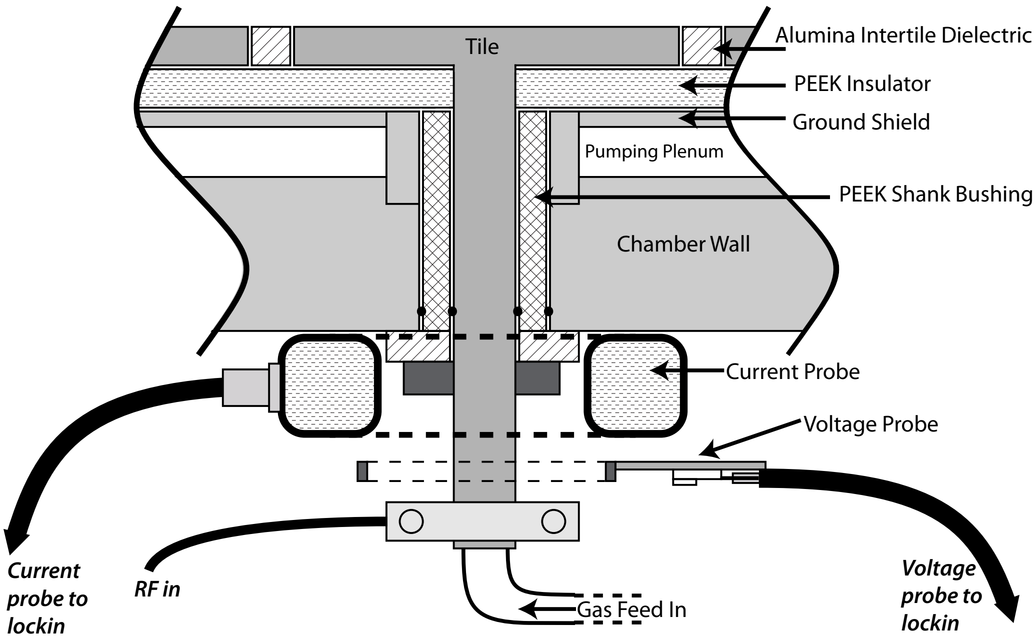

Figure B.1: Showing the current and voltage probe mounted on the electrode shank on the backside of PASTIS

loop in the power splitter. The current and voltage both form standing waves along the electrical path between the power splitter and plasma facing tile surface. A reflection plane exists at the plasma facing tile surface. At the short, current is at a maximum and the voltage is zero. Conversely at the open circuit, current is zero while voltage across the tiles is a maximum. Figure B.2 shows a plot of the current and voltage as a function of normalised position along the electrical path.

We calculate the impedance along the electrical path as the ratio of the voltage and current so that at the open circuit (or at any odd number of half wavelengths), the impedance tends towards infinity. At the short (or similarly at an integral number of half wavelengths) the impedance is zero.

$$V = IR \tag{B.2}$$

$$\lim_{I\to 0} \frac{V}{0} = R \to \infty \tag{B.3}$$

$$or \quad \lim_{V\to 0} \frac{0}{I} = R \to 0 \tag{B.4}$$

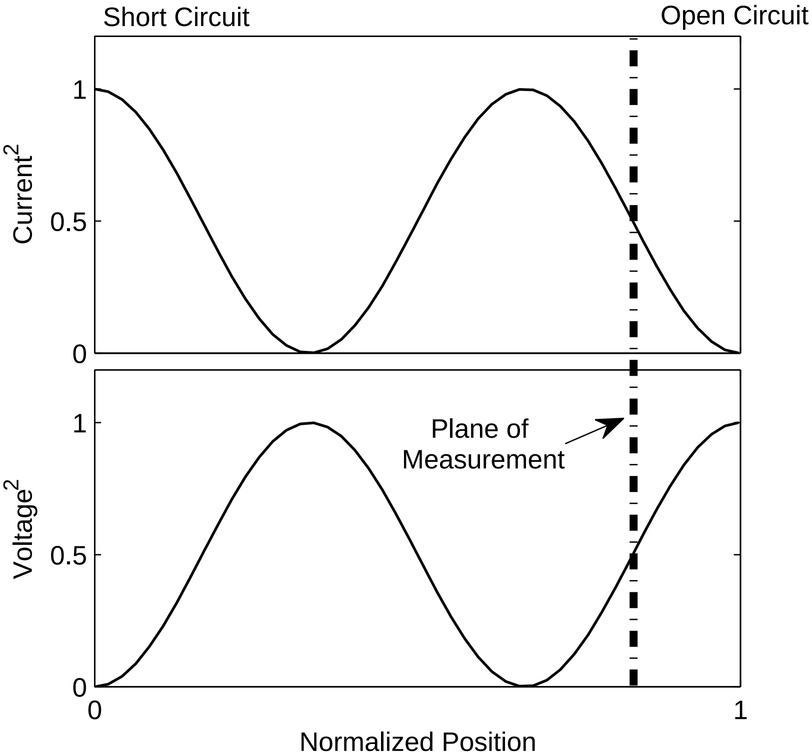

Figure B.2: Magnitude of the current and voltage standing waves as a function of normalised position in the source.

The current and voltage probes are mounted on the electrode shank approximately 10cm away from the plasma facing tile edge (open circuit). Thus the current is now non-zero and the voltage is not at a maximum. See "plane of measurement" in figure B.2.

A decrease in the measured voltage and an increase in the measured current would both directly cause a decrease in the calculated impedance.

$$\frac{V\downarrow}{I\uparrow} = R\Downarrow \tag{B.5}$$

Furthermore as described in section 4.3.2, in vacuum, no current flows along the plasma facing tile edge; whereas in the presence of plasma, the plasma promotes the flow of current into the middle of the tile. Thus there is an increase in the length of the electrical path which must be considered.

The system is no longer an open circuit as the conductive plasma adds a resistive element across the tiles. The current at the plasma facing tile edge is non-zero and the voltage has decreased. As a result, there is a shift in the reflection plane of the standing wave from the tile edge to the tile center (further away from the plane of measurement), thus affecting the measured magnitude of the current and voltages in PASTIS .

Bibliography

[1] B. Chapman, *Glow Discharge Processes Sputtering and Plasma Etching.* Wiley-Interscience, 1980.

[2] M. A. Lieberman and A. J. Lichtenberg, *Principles of Plasma Discharges and Materials Processing.* Wiley-Blackwell, 2005.

[3] A. A. Howling, J. L. Dorier, and C. e. a. Hollenstein, "Frequency effects in silane plasmas for plasma enhanced chemical vapor-deposition," *J. Vac. Sci. Technol.*, vol. 10, p. 1080, July/August 1992.

[4] V. Vahedi, C. K. Birdsali, and M. A. Lieberman, "Capacitive rf discharges modelled by particle-in-cell monte carlo simulation. i: analysis of numerical techniques," *Plasma Sources Sci. Technol*, vol. 4, pp. 261–272, 1993.

[5] V. Vahedi, C. K. Birdsall, and M. A. Lieberman, "Verification of frequency scaling laws for capacitive radio-frequency discharges using two-dimensional simulations," *Phys. Fluids B*, vol. 5, pp. 2719 – 2729, July 1993.

[6] T. Mussenbrock, T. Hemke, D. Ziegler, R. P. Brinkmann, and M. Klick, "Skin effect in a small symmetrically driven capacitive discharge," *Plasma Sources Science & Technology*, vol. 17, April 2008.

[7] M. A. Lieberman, J. P. Booth, P. Chabert, J. M. Rax, and M. Turner, "Standing wave and skin effects in large-area high frequency capacitive discharges," *Plasma Sources Science & Technology*, vol. 11, pp. 283–293, 2002.

[8] A. Ellingboe, "US Patent "Plasma Source" US 7,342,361," March 2008.

[9] T. Michna and A. R. Ellingboe, "N-way power splitting device for a multi-tile segmented electrode plasma source," No. 2010-454, APCPST Proceedings, 2010.

[10] A. Ellingboe, "UK Patent "Power Splitter" GB2458953," April 2008.

[11] Stanford Research Systems, *User's Manual; Model SR844 RF Lock-in Amplifier*, revision 2.4 ed., September 2000.

[12] E. Wang, D. Diebold, and et al., "An improved capacitive divider probe for plasma potential measurements in the phaedrus tokomak," *Rev. Sci. Instrum.*, vol. 62, p. 1494, June 1991.

[13] S. Savas and K. Donohoe, "Capacitive probes for rf process plasmas," *Rev. Sci. Instrum.*, vol. 60, p. 3391, November 1989.

[14] A. Allen and A. R. Ellingboe, "Capacitive probe for measurement of plasma potential oscillation in rf-driven plasma," April 2009. Final Year Project.

[15] K. Ryan and A. R. Ellingboe, "Spatial structure of plasma potential oscillation in a VHF multi-tile electrode plasma source," No. P5-305 in 35th Conference on Plasma Physics, EPS, June 2010.

[16] K. Ryan, D. O'Farrell, and A. R. Ellingboe, "Spatial structure of plasma potential oscillation and ion saturation current in VHF multi-tile electrode plasma source," *Current Applied Physics*, vol. 11, pp. S114–S116, November 2011.

[17] D. J. Griffiths, *Introduction to Electrodynamics*. No. ISBN 0-13-805326-X, Pearson, third edition ed., 1998.

[18] S. Messer, "Broadband calibration of radio-frequency magnetic induction probes," *RevSciInst*, vol. 77, no. 115104, 2006.

[19] R. H. Huddlestone and S. L. Leonard, *Plasma Diagnostic Techniques*. Academic Press, 1965.

[20] P. A. Miller, E. V. Barnat, G. A. Hebner, A. M. Paterson, and J. P. Holland, "Spatial and frequency dependence of plasma currents in a 300mm capacitively

couple plasma reactor," *Plasma Sources Science & Technology*, vol. 15, pp. 889–899, October 2006.

[21] K. Ryan, D. O'Farrell, and A. R. Ellingboe, "A VHF magnetic flux probe as a diagnostic for a large area multi-tile segmented electrode plasma source," No. B6-229, International Conference on the Phenomena of Ionized Gases, August 2011.

[22] R. K. Wangsness, *Electromagnetic Fields.* No. ISBN 0-471-04103-3, John Wiley & Sons, 1979.

[23] T. Rudden, T. Gilmore, and A. Ellingboe, "An investigation into the plasma parameters for a 2-D scalable plasma source for negative-ion production as a possible applicant for neutral beam heating for ITER.," No. C8-298, August 2011.

[24] J. Gudmundsson, Marakhtanov, and et al., "On the plasma parameters of a planar inductive oxegen discharge," *Journal of physics. D, Applied physics*, vol. 33, pp. 1323–1331, January 2000.

[25] J. Gudmundsson, "Notes on the electron excitation rate coefficients for argon and oxegen discharge." Report RH-21-2002, 2002.